INTERPLAY OF MOLECULAR AND NANOSCALE BEHAVIORS IN BIOLOGICAL SOFT MATTER

by

NICHOLAS CIAFFONE

B.S. University of Central Florida, 2016

A thesis submitted in partial fulfillment of the requirements

for the degree of Master of Science in Nanotechnology

in the Nanoscience Technology Center

in the College of Graduate Studies

at the University of Central Florida

Orlando, Florida

Spring Term
2018

Major Professor: Laurene Tetard

ABSTRACT

The complexity of biological soft matter at the sub-micrometer level is fundamentally correlated to the functionalities at the larger scale. Reflecting the level of heterogeneities in the properties of systems remains challenging when probing small scales, due to the mismatch between the area surveyed with the tools offering nanoscale resolution, such as atomic force microscopy (AFM), and the scale of natural variations inherent to biology. Hence, to understand the physiological and mechanical alterations that occur within a single cell relative to a cell population, a multiscale approach is necessary.

In this work we show that it is possible to observe molecular, chemical and physical alterations in both plant and human cells with a multiscale approach. Biophysical and biochemical traits of cell populations are studied with Fourier Transform infrared spectroscopy (FTIR) and in turn, guide higher resolution discovery with Raman spectroscopy and nanoscale infrared spectroscopy using AFM (NanoIR) to access finer details. We illustrate this with three examples of biological soft matter systems: 1) a preliminary study of cellular interactions with naturally occurring vehicles applicable to human health, 2) a qualitative examination of antibiotics and new pesticide treatments in food crop systems, and 3) a fundamental investigation of the deconstruction mechanisms of plant cells during pre-treatments in preparation for biofuel production.

Keywords: Soft Matter, Raman Spectroscopy, Atomic Force Microscopy

ACKNOWLEDGMENTS

This thesis would not have been possible without the support of many people, mainly my thesis chair and mentor, Dr. Laurene Tetard, who gave me the opportunity to follow my dream to pursue research, encouraged me to advance my career with this Master's program, as well as reading numerous revisions and last but not least, guiding me to become the scientist and leader I am today. I would also like to extend my gratitude to my other committee members, Dr. Hyeran Kang and Dr. Swadeshmukul Santra, both of whom offered guidance and support. I would also like to thank Dr. Kiminobu Sugaya for providing me with an opportunity to investigate cellular interaction phenomena that occurs between HEK 293 cells and their exosomes. Without his shared curiosity for nanoscale investigation of human cells, my thesis advancements would not be possible. In addition, the research performed was an inclusive effort conveyed by many talented scientist, but could not have been possible without the boundless scientific minds of all my lab mates Mikhael Soliman and Briana Lee that helped me tirelessly throughout my Master's tenure. Throughout my experience at the NanoScience Technology Center, I have learned numerous techniques and experimental protocols associated to nanoscale characterization, which I intend to use in my future career. Additionally, I want to thank the University of Central Florida and NanoScience Technology Center for providing an environment that allows students to express their potential in the realm of scientific knowledge. Lastly, thank you to my parents, and numerous friends who stood by me, through thick and thin, always offering love and support. Their advice and direction has been invaluable during this process and their words of encouragement created a platform for me to build a promising future upon.

TABLE OF CONTENTS

LIST OF FIGURES

LIST OF TABLES

LIST OF ACRONYMS (or) ABBREVATIONS

1x PBS	One Time Diluted Phosphate Buffer Solution
a.u.	Arbitrary Unit
ACP	Asian Citrus Psyllid
AFM	Atomic Force Microscopy
ATR	Attenuated Total Reflectance
Au	Gold
ºC	Degrees Celsius
CaF_2	Calcium Fluoride
CCD	Charge Coupled Device
CD63	Cluster Differentiation 63 Antigen
*C*Las	*Candidatus* Liberibacter asciaticus
CM^{-1}	Unit of Wavenumber
CO_2	Carbon Dioxide
dH_2O	Deionized Water
DMEM	Delbarcco's Modified Eagle Medium
DNA	Deoxyribonucleic Acid
E	Energy
e.g.	Examples Given
E_0	Ground State of Energy
EDTA	Ethylenediaminetetraacetic acid
EM	Electron Mircoscopy
EPA	Environmental Protection Agency
FBS	Fetal Bovine Serum
FTIR	Fourier Transform Infrared Spectroscopy
g/mm	Grooves Per Millimeter
H_2SO_4	Sulfuric Acid
HEK 293	Human Embryonic Kidney Cell Line (293^{rd} experiment)
HLB	Huanglongbing
Hz	Hertz
IR	Infrared
KHz	Kilohertz
L-Glutamine	Laevus Glutamine
M	Molar
mg	Milligram
mL	Milliliter
mg/mL	Concentration in Milligrams per Milliliter
mm	Millimeter
Mid-IR	Mid-infrared spectroscopy
min	Minutes
MVB	Multi-Vesicular Body
mW	Milliwatt
µL	Microliter
µm	Micrometer
N/M	Newtons Per Meter

NaCl	Sodium Chloride
NanoIR	Nanoscale Infrared Spectroscopy
nm	Nanometer
OTC	Oxytetracycline
PBS	Phosphate Buffer Solution
PC	Principal Components
PCA	Principal Component Analysis
PEG	Polyethylene Glycol
pH	Potential of Hydrogen
RNA	Ribonucleic Acid
RPM	Revolutions Per Minute
s	Second
SERS	Surface Enhanced Raman Spectroscopy
SNAP-TAG	Synapylsomal Associated Proteins
SPM	Scanning Probe Microscopy
TEM	Transmission Electron Microscopy
THF	Tetrahydrofuran
UF-IFAS	University of Florida- Institute of Food and Agricultural Sciences
wt	Weight

CHAPTER ONE: INTRODUCTION

1.1 Introduction

From the point of view of analytical characterization, biological systems such as cells are considered as soft matter – a subset of condensed matter. Soft matter has been defined as "a physical system that can evolve out of equilibrium due to stresses at the level of thermal fluctuations" (Hamley, 2013). The resulting alterations caused by external factors can be observed in the form of biochemical, biophysical and morphological changes. To probe such alterations, traditional microscopy is not sufficient mainly due to the limitation in spatial resolution, around half of the wavelength according to Abbe's diffraction limit (Abbe, 1874).

1.2 The importance of Nanoscale Characterization in Soft Matter Systems

Soft matter systems in biology exhibit very complex and intricate interactions at the molecular levels, which affect the behavior of entities at the micro-, meso- and macro-scales. Nanoscale characterization using various microscopy and spectroscopy techniques have been widely used in biological media such as in plant systems to map the composition distribution of lignin and cellulose in cell wall structures (Chundawat et al., 2011; Tetard et al., 2010), or track nanoparticle through plant systems (Yang et al., 2016), as well as in mammalian cells to investigate mechanical responses of stem cells to stimuli (Janmey & McCulloch, 2007) or to asses pathologies such as with carcinoma cells (Lasch, Haensch, Naumann, & Diem, 2004).

The main limitation, to date, is in the development of tools to probe nanoscale properties of the living systems, beyond morphology. However, recent advances in nanometrology made it possible to explore new properties of living systems. For instance, atomic force microscopy (AFM)

to investigate biomechanics of delignified Poplulus as a result of biomass extraction (Tetard et al., 2011). Surface enhanced Raman spectroscopy (SERS) has been shown to be sensitive to protein interaction (Hackett, Li, Ameen, Goddard, & Liu, 2018) while, Raman spectroscopy has been utilized to study cellular uptake of tagged fatty acids (Jamieson et al., 2018). With the ability to access physical and chemical changes occurring in plants and mammalian cells experiencing external stresses establishing correlations with the behavior of the same systems at various scales becomes achievable.

1.3 Nanoscale Entities in Soft Matter Systems

In the past few decades, biological assays have been developed to qualitatively and quantitatively measure protein (<10 nm), DNA (1-2 nm) and RNA (1-2 nm) content within a cell. This includes investigating the miRNA content of exosomes using real time polymerase chain reaction (Chevillet et al., 2014), mapping of surface proteins on exosomes using Western blotting (Théry et al., 2001), and using complementary DNA microarray to track alterations in tomato plants when introduced to toxins (Frick & Schaller, 2002). Although these bioassays have enabled major advancements in our understanding of biological processes, they remain limited in the capability to study single cells. The results from these bioassays constitute an average response of the population probed during the test at hand. In studies aiming at monitoring alterations of carbohydrates occurring at the plant cell wall level, bioassays will not support the identification of specific elements associated with the treatment, nor will they help tracking movement of a molecule or particle across a biological system.

Changes of these components, although occurring on a small scale, may have large implications and therefore should also be observed in reactions. In order to observe subcellular

alterations, sensitive measurements must be implemented. Previous reports in the literature show that Fourier Transform Infrared Spectroscopy (FTIR), Raman spectroscopy, AFM, and nanoscale infrared spectroscopy (NanoIR) all possess some advantages to characterizing various aspects of the subcellular alterations of biological systems such as organelles. For instance, Raman spectroscopy has been used for characterization of subcellular components in plant cell walls (Agarwal, 2006), while AFM has been used to investigate single mammalian cell transfection using specialized probes (Cuerrier, Lebel, & Grandbois, 2007). In plants, IR spectroscopy and NanoIR imaging have been employed in tandem to capture the process occurring upon pre-treatments (Tetard, Passian, Farahi, Thundat, & Davison, 2015; J. Wang et al., 2017).

In addition, a review of the literature suggests that chemometrics, such as principal component analysis (PCA) or neural network should be implemented to take into account the variability of the changes observed in such complex systems with natural variability. This has been shown to be important to differentiate cell gene expression (Yeung & Ruzzo, 2001), determining biomarkers for lymphoma cell lines (Verhoeckx et al., 2004), detecting minute differences in soft wood materials (Hori & Sugiyama, 2003) and many other applications.

1.3.1 Chemical Alterations

The composition of biological tissues is often indicative of its integrity and functionality. A biological system's response to stress often involves a change in the chemistry of the system. Some examples include tracking responses of cytotoxicity caused by silver nanoparticles using Raman spectroscopy (Singh & Ramarao, 2012), stress responses to nutrient deficiencies using FTIR in plant cells (Stehfest, Toepel, & Wilhelm, 2005), alterations due to pathologies such as

cancerous cells (D. Yang et al., 1995) or chemical changes after biomass extraction treatments (F. Xu, Yu, Tesso, Dowell, & Wang, 2013).

From our review of the literature, several instruments seem to be rather common to study the changes in composition, such as several variations of mass spectrometry (Palmer, Ashton, & Moncada, 1988; Sharma et al., 2004), nuclear magnetic resonance (Laulagnier et al., 2004; Ralph, Ralph, Landucci, & Landucci, 2004), infrared spectroscopy (Emmanuel, Odile, & Céline, 2015; Matthäus et al., 2008), Raman spectroscopy (Gierlinger, Keplinger, Harrington, & Schwanninger, 2013; Lin et al., 2013), carbohydrate microarray(Moller et al., 2008; D. Wang, Liu, Trummer, Deng, & Wang, 2002), carbohydrate gel electrophoresis (Barnes et al., 2016; Goubet, Jackson, Deery, & Dupree, 2002), and capillary electrophoresis (Croset et al., 2012; Vaher & Koel, 2003).

In the present work, we will focus on FTIR spectroscopy as it is a powerful tool to study changes in composition in biological systems. The chemical bonds, or covalent bonds resulting from sharing of electrons in the valence shell (Cooper, 2002) of two atoms, can be modeled as a mass-spring-mass systems. Covalent bonds make up more complex structures in the form of molecules and polymers, which are very abundant in soft matter. Molecular bonds can vibrate absorbing energy from incoming photons. When the incoming light covers a range of energy corresponding to the various vibrational modes ($4000cm^{-1}$-$400cm^{-1}$) in the molecules or polymers, an infrared (IR) spectrum (usually several IR bands) is formed corresponding to the unique fingerprint of the system probed. Monitoring the variations in IR fingerprints can then be used to determine the nature of a reaction/change occurring in the system. By studying changes in amplitude or position of the IR bands, it is possible to understand what alterations occur in the system at the molecular level.

IR spectroscopy methods encompass mid-infrared spectroscopy and Raman spectroscopy, which will be explained in more details in Chapter 2. Although mid-IR spectroscopy is limited in spatial resolution (Kačuráková & Wilson, 2001), recent advances in metrology have brought about a platform for nanoscale measurements (Dazzi, Prazeres, Glotin, & Ortega, 2005) of molecular vibrations resulting from infrared excitation of the sample, which will also be discussed in Chapter 2.

1.3.2 Physical Alterations

Biomechanics features, such as cellular rigidity and cell adhesion, play important roles in cellular behavior (Brunner, Niendorf, & Käs, 2009; Costa, 2004; Lee & Lim, 2007). Although components involved in rigidity and structural support differ in plant and cell walls, it has been observed that removal or alterations of these components can also cause significant change in physiological processes. For instance, cell rigidity in cucumber plants upon selected treatments (Adatia & Besford, 1986), or understanding the important role of cell adhesion in growth of non-woody plant tissues (Jarvis, Briggs, & Knox, 2003) have been reported. Alterations of biomechanical properties in mammalian cells have been used to understand pathologies such as malaria and gastrointestinal cancer (Suresh et al., 2005), or skin cancer (Runge et al., 2014).

Morphological changes are the easiest to assess through characterization techniques such as AFM and electron microscopy (EM). As an example, morphological changes such as membrane disruptions, which occur in cell endocytosis of lipopolyamines, have been captured using electron microscopy (Labat-Moleur et al., 1996). More dramatic morphological changes such as those taking place during cell apoptosis have been observed using transmission electron microscopy (TEM) (Brunk, Dalen, Roberg, & Hellquist, 1997) while structural changes in lymphocytes caused

by apoptosis have been studied with AFM (Hu, Wang, Zhao, Dong, & Cai, 2009). Alterations in cornstover cell morphology after deconstruction of structural polymers from biomass extraction treatments have also been observed using EM and AFM (Chundawat et al., 2011).

Our literature review suggests that nanomechanical measurements have greatly benefited from AFM, especially force measurements. From this approach, Young's modulus, adhesion and energy dissipated during the tip-sample interaction can be used to monitor changes in the system. In mammalian cells, force measurements have been used to assess the differences in Young's modulus between different cell types (Alcaraz et al., 2003; Mathur, Collinsworth, Reichert, Kraus, & Truskey, 2001). Later, this approach was also used to understand cell alterations in pathologies such as cancer (Cross, Jin, Rao, & Gimzewski, 2007; Faria et al., 2008; Q. Li, Lee, Ong, & Lim, 2008). Elastic properties of plant cells walls have also been studied with this approach (Benıtez, Matas, & Heredia, 2004; Touhami, Nysten, & Dufrêne, 2003).

1.4 Summary and thesis preview

In this thesis, we study the biomechanical and biochemical traits of biological materials under various conditions. These materials will be investigated using Raman spectroscopy, FTIR, AFM, NanoIR and chemometrics techniques such as PCA. A detailed overview of these techniques will be provided in Chapter 2. Chapter 3 will discuss a multiscale approach to observe the pathways and alterations occurring between Human Embryonic Kidney cells (HEK 293) cells and their exosomes to determine uptake method and information transfer in the form of protein synthesis and nucleic acid intensity shifts. Chapter 4 will discuss multiscale approach to investigate plant cells. Two examples will be discussed, including the effect of a co-solvent combined with heat treatment for the development of efficient biofuel extraction, and the uptake of therapeutics across

leaf membranes for the purpose of combatting emergent bacterial plant diseases. Chapter 5 will provide a summary of our findings and an outlook on the potential of nanoscale characterization for soft condensed materials.

CHAPTER TWO: INSTRUMENT THEORY

2.1 Vibrational Spectroscopy

Over the past 50 years, a surge of studying cellular structures has emerged mainly thanks after the isolation of green fluorescence protein, which makes it possible to tag selected cell structures for optical imaging (Shimomura, Johnson, & Saiga, 1962). Confocal microscopy and two photon microscopy (Diaspro, 2001) are two important platforms for such studies. More recently, labeling cells with highly specific proteins and nanoparticles such as the use of synapylsomal associated protein (SNAP-Tag) protein has also been considered for imaging using fluorescence microscopy (Srikun, Albers, Nam, Iavarone, & Chang, 2010) or bio-conjugating quantum dots for organelle specific labelling can be considered for imaging as well (Medintz, Uyeda, Goldman, & Mattoussi, 2005). However, there are limitations to labelling including photo bleaching, weak specificity of certain dye binding sites, added incubation times, or need for harsh solvents for storage. All of these limitations may be overcome in time. One of the largest problems to consider with labelling procedures, however, is the possibility of alterations to the cell state due to binding conformation shifts or interactions with inorganic materials in the case of many quantum dots or nanoparticles.

On the other hand, vibrational spectroscopy methods such as Raman and mid-infrared spectroscopy offer label-free molecular characterization of samples, making them attractive alternatives to traditional fluorescence methods. However, their use is not as widespread as fluorescence, partly due to the cost of the equipment and the more complex analysis required upon data collection. Next, we discuss the principle and operation of the IR spectroscopy methods used for the work presented in Chapter 3 and 4.

2.1.1 Vibrational Modes

Molecular vibrations are observed when a bond absorbs the energy (E) corresponding to the resonance of the mass-spring-mass system representing the covalent bond in a molecule. Each molecule with more than two atoms will generally exhibit vibrational modes at different energies. These vibrational modes or frequencies are dependent on bond strength and on the mass of atoms. Some of the most common vibrational modes can be found in figure 1.

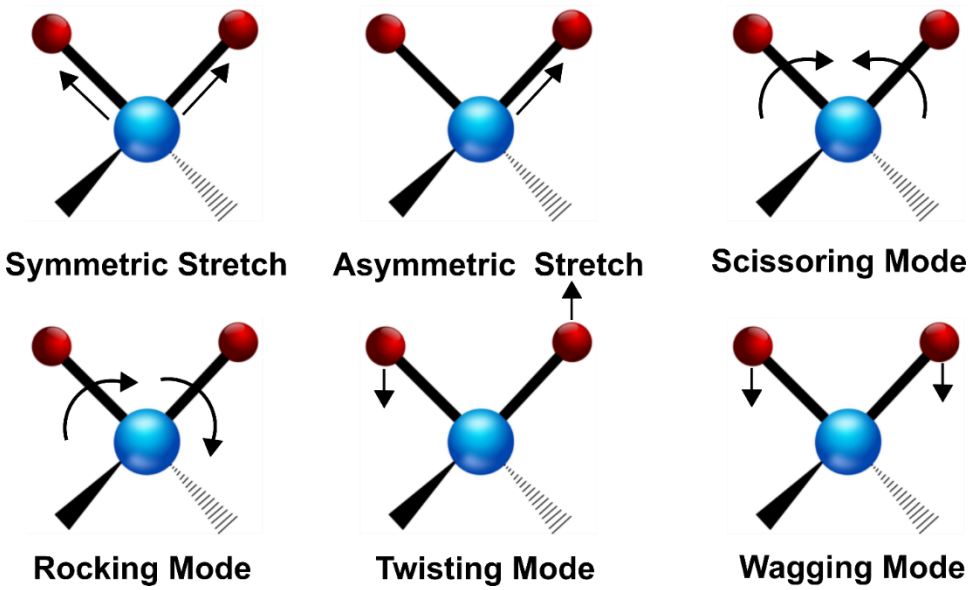

Figure 1: Illustration of the Vibrational Modes Resulting from the Multiple Degrees of Freedom in a Molecule. Stretching mode can be symmetric stretching i.e. bonds vibrate at the same time, or asymmetric i.e. bonds stretching alternates. In bending modes (wagging, twisting, scissoring), the displacement is likely in the out-of-plane direction.

2.1.2 Inelastic and Elastic Light Scattering

Vibrational modes in a molecule can be probed using an incident light in the infrared range, for energetic transition to lay in the vibrational range: the incoming energy will excite the system from ground state to excited state, leading to the molecule to vibrate. The energy released as the molecule decays back to ground state is usually dissipated to the lattice in the form of heat. This

approach is referred to as mid-IR spectroscopy, carried out with a Fourier transform infrared spectrometer. Another method to probe the fingerprint of the material is to use an incident light with higher energy, usually in the visible range. This excites the system from its ground state to a virtual state, much higher than vibrational state. The light scattered from this process contains photons with several energies: i) photons with same energy as the incident light (Rayleigh or elastic scattering), which corresponds to photons emitted when the system decayed from the virtual state back to the same ground state; ii) photons with less energy than the incoming photon (inelastic scattering, or Stokes scattering) as the system decays to an energy level that is a little higher than the original ground state. The difference in energy holds information of the vibrational modes of the system, and iii) photons with more energy than the incoming photon (inelastic scattering, or anti-Stokes scattering) as the system decays to an energy level that is a little lower than its original state. A summary of the transition is provided in figure 2.

Although Rayleigh scattering is the most common transition it is possible to isolate photons resulting from inelastic scattering. The Raman effect, which corresponds to inelastic light scattering, occurs when a monochromatic light source of wavelength λ_0 (or frequency f_0) scatters off of a material with a different wavelength λ_1.

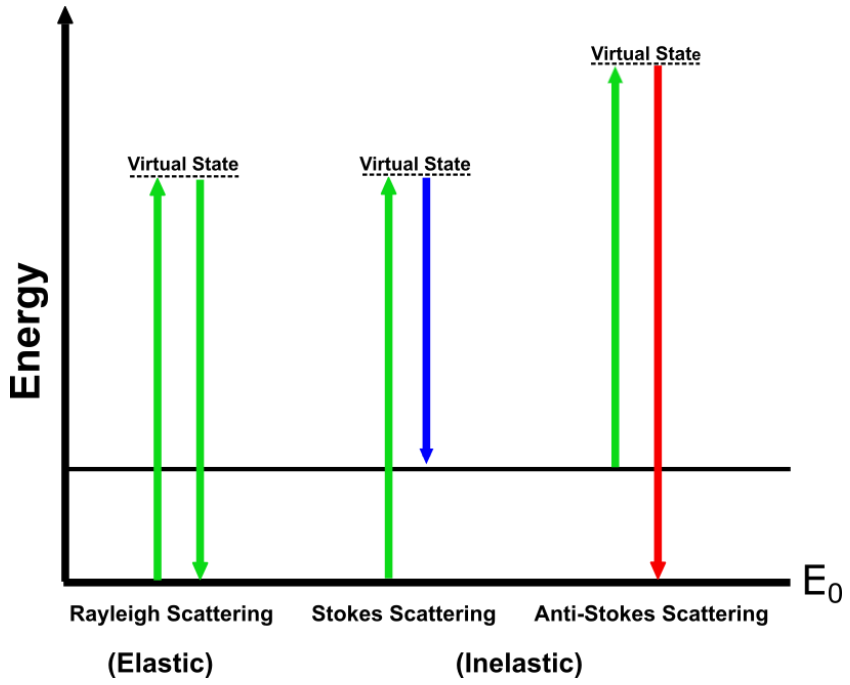

Figure 2: Jablonski Diagram of Light Scattering Patterns. Rayleigh scattering, also known as elastic scattering corresponds to an incident light exciting the sample in its ground state E_0 to virtual state, and collecting the photon emitted as the system decays back to its ground state E_0. Raman (inelastic) scattering the photon is emitted as a result of a decay to a state slightly above the ground state, which corresponds to vibrational transitions of the system. In anti-Stokes scattering, the excited photon state holds slightly higher energy than the ground state.

2.1.3 Raman Spectroscopy

Raman spectroscopy is a powerful molecular "fingerprinting" technique revealing the molecular vibration of materials (Hanlon et al., 2000) based on inelastic scattering. Because of the excitation in the visible range, it is possible to focus the light with a microscope objective down to a few hundred nanometer (laterally) focal point. Hence, this vibrational spectroscopy technique offers relatively high spatial resolution. By coupling this technology with confocal microscopy, it is also possible to control the depth probing for subsurface measurements (Anderson, Anger, Hartschuh, & Novotny, 2006; Eliasson, Claybourn, & Matousek, 2007). Raman spectroscopy has recently gained traction as a method for molecular fingerprinting of biological samples (Agarwal, 2006; Agarwal, McSweeny, & Ralph, 2011; Hanlon et al., 2000; Matthäus et al., 2008; Pérez et

al., 2016), particularly when resolving features or variations at the sub-micrometer level is of interest. Rapid and sensitive disease detection (Graham et al., 2011; Koyner et al., 2010; Kristiansen et al., 2003; Pérez et al., 2016; L. Xu et al., 2015), as well as understanding fundamentals components of cells (Agarwal, 2006; Matthäus et al., 2008; Zhang et al., 2012) have been tackled with Raman confocal imaging. Hence, Raman spectroscopy may be an important part of understanding, tracking, and optimizing man-made processes in biological systems.

2.1.3.1 History of Raman Spectroscopy

The study of inelastic light scattering was first theorized by Smekal in 1923 (Ferraro, 2003), and observed in 1928 by Sir CV Raman and Krishnan (Raman & Krishnan, 1928), who coined the scattering with his name. It is important to note that Raman scattering effect only occurs in roughly 1:1,000,000 photons of scattered light. This prevent the process to be studied until the invention of the stable and powerful lasers, to produce a sufficiently large amount of scattered light photons.

2.1.3.2 Raman Spectroscopy Principle and Setup

As previously mentioned, Raman confocal spectroscopy has been used extensively to characterize biological samples such as mammalian (Lin et al., 2013; Matthäus et al., 2008; Whelan et al., 2011) and plant cells (Agarwal, 2006; Gierlinger et al., 2013; Larsen & Barsberg, 2010). In short, the sample is excited with a monochromatic laser beam focused on a region of interest. The inelastic light scattering off the molecular vibrations is then collected with the microscope objective in up-right configuration. Rayleigh scattering is suppressed with a notch filter blocking the excitation wavelength prior to entering the spectrometer. In the spectrometer, the photons are counted by wavelength using as diffraction grating (600 grooves per millimeter

(g/mm) in this work). The photons are then detected and analyzed using a charge coupled device (CCD) detector (Boyle & Smith, 1970). The CCD detector contains photosensitive elements which create a charge when hit by a photon corresponding to the intensity of the photon and converted using software (WITec Control FOUR, Ulm, Germany). The scattered signals can be collected at selected arrays of points to gather a chemical map of the area of interest. A schematics of the setup is provided in figure 3.

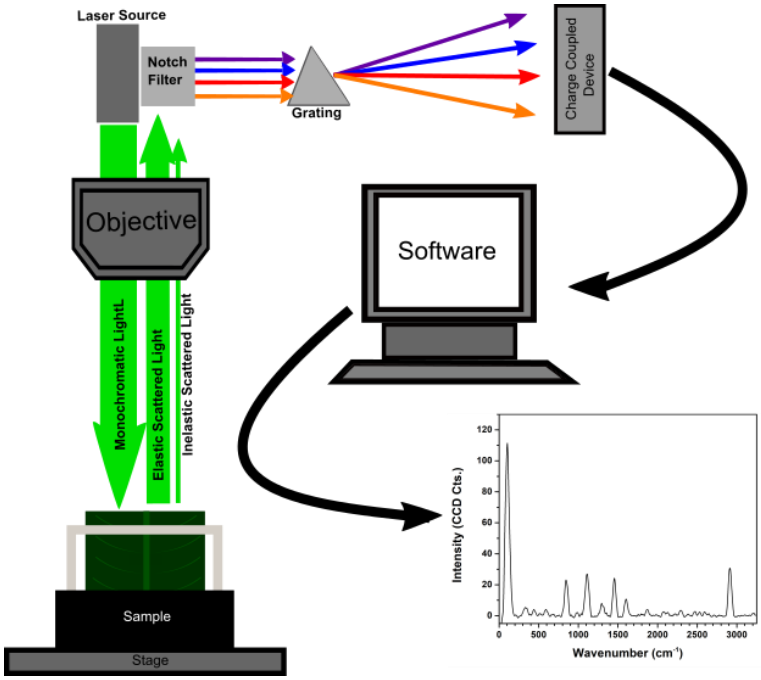

Figure 3: Schematic Representation of Raman Spectroscopy. Excitation laser (532 nm) excites a sample. Light is focused onto the sample using an optical objective (20x, 50x or 100x). Scattered light is collected with the same objective. Elastic scattered light is filtered with a notch filter. The remaining photons are split with a 600 g/ mm grating. A CCD detector in which photon sensitive semiconductor elements detects photons are used to collect the spectra. The resulting photon charges as a function of wavelength are converted to spectra representing the molecular fingerprint of a sample.

In the system used to produce the data presented in this work (Witec 300 RA), the implementation of the spectroscopy on a confocal microscope, using a two pinhole arrangement that restricts both depth and lateral size of sample volume probed, increases the lateral spatial

resolution, δ_{lat}. This has been expressed by equation (Sijtsema, Wouters, De Grauw, Otto, & Greve, 1998):

$$\boldsymbol{\delta_{lat} = \frac{0.62\lambda}{NA}} \quad (1)$$

As can be seen from the equation, the spatial resolution is dependent on laser wavelength, and numerical aperture (NA) of the objective. In our system, the wavelength of the incoming laser was fixed at 532 nm and objectives with 20x/ 0.4 NA and 100x/ 0.9 NA magnification were used.

2.1.4 Mid-infrared (Mid-IR) spectroscopy in the form of Attenuated Total Reflection Fourier Transform Infrared Spectroscopy (ATR-FTIR)

Mid-infrared (Mid-IR) spectroscopy is another approach to measure the molecular fingerprint of a material. Mid-IR absorption involves transitions between vibrational energy states and rotational sub-states which make it possible resolve bending and stretching modes of a bond and assign them to specific functional groups. Mid-IR approaches require a IR illumination source. For lack of mature IR laser technologies, IR systems are generally comprised of IR radiative light such as black body sources. The first generation of IR systems consist of a monochromator and detector to measure the absorption in the material. However, this time-consuming method was replaced by FTIR spectrometers, the principle of which will be discussed next.

2.1.4.1 Fourier Transform Infrared Spectroscopy Principal, Setup and ATR Configuration

Infrared spectroscopy measures the absorption of photons through a medium (the sample). In FTIR spectroscopy, the light source is a diffusive black body source emitting in the spectral range 2.5 µm to 50 µm. Photons with sufficient energy excite the vibrational transition of molecules, as previously described in section 2.1.2. The position and intensity of molecular

vibrations are in part related to bond strength, mass of the atom in molecular vibration and concentration of the molecule in the medium probed.

In FTIR, the spectrum is obtained using a Michelson interferometer (figure 4). The light emitted is split in two beams by a beam splitter. Half the light is directed toward a fixed mirror reflecting back towards the beam splitter while the other half of the light is directed towards a moving mirror and reflected back to the detector. The mirror motion introduces an optical path difference (OPD). When the beams recombine, the OPD leads to the formation of constructive and deconstructive interference. This pattern is referred to as interferogram. As the light interacts with the sample, the energy corresponding to the molecular vibrations in the material is absorbed. Hence the light transmitted corresponds to the interferogram, with missing energies. This is captured by the IR detector. The interferogram (Intensity vs. OPD) data is processed using the software to perform the Fourier transform which produces the IR spectrum (Intensity vs. Wavenumber).

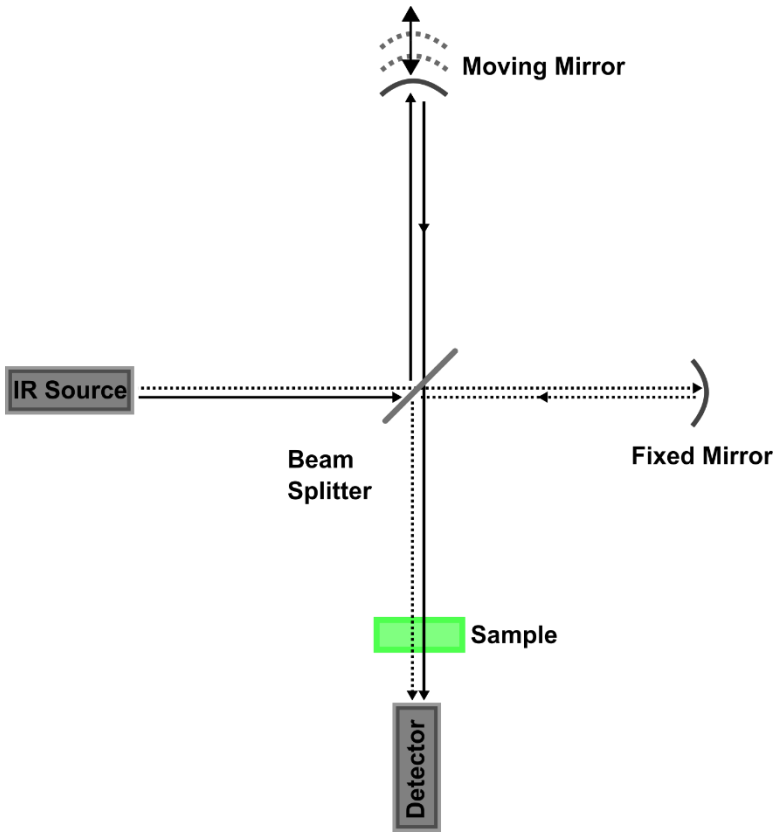

Figure 4: Representation of the Michelson Interferometer in Fourier Transform Infrared Spectroscopy. An incident beam of light is split by a beam splitter: one half is directed towards a fixed mirror, while the other half is directed towards a moving mirror. The split beams recombine at the beam splitter to the sample and the detector.

Attenuated total reflectance (ATR) involves routing the light through a highly refractive substrate to create the conditions for total internal reflection by causing an evanescent wave at the surface of the prism-sample interface, (Fahrenfort, 1961) as shown in figure 5. The ATR surface used in this thesis is diamond covered zinc selenide. Zinc selenide is an ideal candidate since it is an IR transparent material. As it but is easily scratched, diamond is used on the surface due to its robust nature and scratch resistance. However, diamond does contain peaks in the 400 cm^{-1}-4000cm^{-1}. The transmission of diamond is removed in the background subtraction to prevent

interference in spectra. The evanescent wave in ATR has the ability to penetrate the sample between 0.5 µm-2µm.

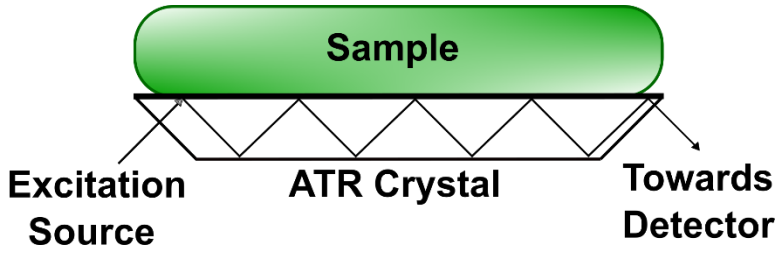

Figure 5: Attenuated Total Reflectance (ATR) Setup. Infrared radiation enters the ATR crystal with a specified angle for evanescent wave formation. The evanescent wave is formed at each reflection at the surface of the prism. As the light exits the prism, it is directed towards the FTIR detector to collect the infrared spectrum.

2.1.5 Selection Rules for IR Spectroscopy and Raman Spectroscopy

Mid-IR and Raman spectroscopy techniques are both based on excitation of the vibrational modes to obtain the chemical fingerprint of a sample. However, they are both subject to selection rules (originating from quantum mechanics). In brief, Raman scattering is observed in molecules observing a change in polarizability upon a given molecule vibration. IR spectroscopy on the other hand requires a change in a dipole moment caused by absorption of light by the vibrating molecule to be active. For example, water exhibits several intense IR bands in the 4000 – 400 cm^{-1} range due to the change in dipole moments experienced with the different types of vibrations, while Raman scattering are limited to fewer modes (Matthäus et al., 2008).

2.2 Atomic Force Microscopy (AFM)

2.2.1 History of AFM

With the introduction of scanning tunneling microscopy (STM) in the 1982 (Binnig, Rohrer, Gerber, & Weibel, 1982) and AFM in 1986 (Binnig, Quate, & Gerber, 1986), nanoscale

characterization of biological samples in their natural state became possible. Today, AFM goes beyond morphological characterization and with advanced nanomechanical and nanochemical properties, to name a few. (Benıtez et al., 2004; Cross et al., 2007; Wagner & Mueller, 2016)

2.2.2 Atomic Force Microscopy Principle and Setup

AFM uses a microcantilever to probe the sample properties. At the end of the cantilever beam, on the bottom side, a tip of just few atoms in diameter is fabricated to provide the local interaction with the sample. The cantilever is then moved across the sample surface and the deflection of the cantilever interacting with the sample surface is registered by a laser reflected off the back of the cantilever into a photodiode detector. This detector records the variations in deflection, the computer indexes the deflection as a function of position to create images representing the tip-sample interaction. The process of AFM scanning can be visualized in figure 6.

The two main modes of AFM imaging are: contact mode and tapping mode. With contact mode, the tip-sample distance is small – sometimes reaching Pauli exclusion limit. In this operation, “constant force feedback” is commonly used: the force the cantilever applies to the sample is kept constant by the adjusting the tip-sample distance by electronic feedback using the gains parameters in the control panel. Although suitable for many applications, contact mode can be harsh on the sample surface and sometimes damage the surface as the tip rasters the sample. This is specially challenging for soft materials. Hence other modes of imaging have been developed to circumvent this limitation.

In Tapping mode (or AC mode) the tip-sample distance is modulated to limit the contact to a gentle “tap” on the sample. The oscillation of the cantilever is obtained with a piezoceramic

piece actuated at a frequency and amplitude tuned to match the resonance of the cantilever. It has previously been shown that minute changes in the properties of the materials can be distinguished using this approach in addition to the high resolution topography images produced.

Quantitative information such as adhesion, stiffness, Young's modulus and height of a sample can be determined. In most cases, the simplest model considered for these analysis is Hooke's law, as shown in equation 2:

$$\boldsymbol{F = -k\Delta x} \qquad (2)$$

where F is the force generated by the cantilever, k is the spring constant (N/m), and Δx is the displacement (m) of the cantilever for the given force F (N).

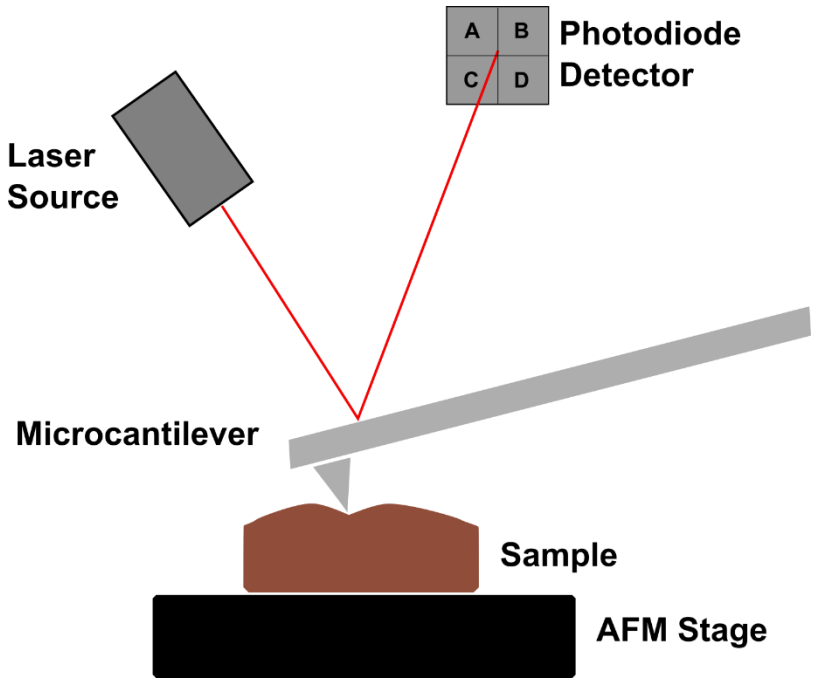

Figure 6: Schematics of the Atomic Force Microscope. AFM utilizes a microcantilever with a sharp tip. The probe of the cantilever rasters the sample deflecting and bending based on changes in the tip-sample interaction. These changes can then be mapped by a laser reflecting off the back of the cantilever to a photodiode detector. An image can be generated based off the changes in signals recorded. The Atomic Force Microscope (AFM) is used to obtain nanoscale topography images of a sample surface. Beyond morphology, mechanical or chemical properties can now be attained.

2. 3 Nanoscale Infrared Spectroscopy (NanoIR)

As discussed earlier in the chapter, one of the largest setbacks associated with IR spectroscopy is spatial resolution. NanoIR is an instrument that combines the use of AFM and IR for nanoscale resolution was first reported in 2005 (Dazzi et al., 2005). Since the first report, the platform has been commercialized for widespread application. Today, it is possible to probe samples for chemical mapping of structures down to the nanoscale (Tetard et al., 2015).

2.3.1 NanoIR Setup and Theory

A combination of traditional AFM with IR spectroscopy allows for nanochemical mapping of a sample. The principle is based on photothermal expansion generated in a material as a result of exciting its vibrational modes. We first obtain an AFM image of the desired location. Then, the IR laser (Quantum Cascade Laser from Daylight Solutions) that is focused on to the sample using a curved Au-coated mirror is aligned below the cantilever tip by pulsing the light at the contact resonance of the cantilever, at a wavelength that creates photothermal expansion in a calibration sample of known absorption (such as PMMA). When the infrared laser is set at a wavelength corresponding to its vibrational mode, energy absorbed by the sample with be released to the lattice in the form of heat, in turn leading to photothermal expansion of the sample. By measuring the amplitude of the expansion of the sample at the frequency of the laser pulse using the cantilever deflection and photodiode detector, as in AFM, it is possible to reconstruct a chemical map of the sample. This process can be visualized in figure 7. Another possible measurement with this platform is to fix the position of the cantilever and sweep the wavelength of the laser. Recording Amplitude vs. Wavelength corresponds to the localized IR spectrum of the material. Nanoscale resolution well below 100 nm has previously been demonstrated for finite structure with a homogeneous composition (Tetard et al., 2015).

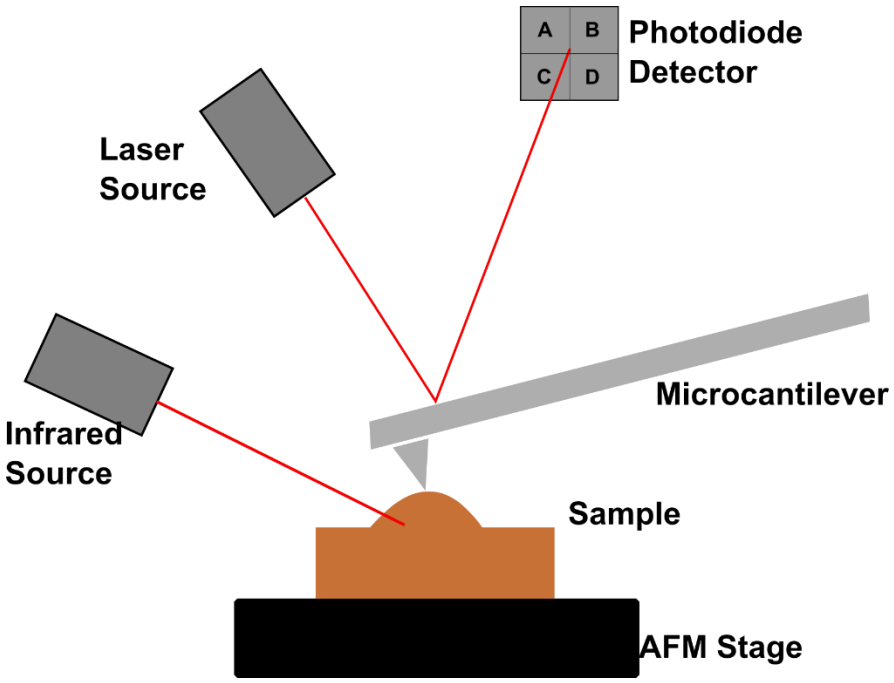

Figure 7: Schematic of Nanoscale Infrared Spectroscopy (NanoIR) Spectroscopy. Infrared laser exciting a sample causes heat expansion when the photon energy matches with the vibrational modes of the material. The photothermal expansion can then be detected by measuring the change in AFM cantilever deflection with the AFM photodiode detector. This change in deflection can then be converted to IR spectra with observed peaks correlating to absorption of IR at a particular wavelength.

2.4 Principal Components Analysis

Principal components analysis is a multivariate method of data analysis and classification that can be used to represent a large dataset with multiple variables into a new reference frame in which the first principal components represent the direction of largest variations in the dataset (Bro & Smilde, 2014). The dataset is treated as a matrix. Eigenvectors of the matrix are calculated for the matrix to be plotted on a mutually orthogonal plane. A principal component corresponds to an eigenvector of the matrix. Each principal component is scored in indication of the variance captured. Principal components 1 and 2 usually capture the highest variations in the dataset considered in this work. The distribution of the data points in the new reference frame using

principal components as the axes are then considered in 2D or 3D plots, depending on the score of the principal components. This means that a difference in distance between two points on the x axis (PC1) correlates to a larger difference between data sets than a difference between data sets on the y axis (PC2), and so on (figure 8). Each plot on the graph represents a spectrum, or average of spectrums of the data. A clustering of points suggests a high correlation between data points. For example, a group of cells including untreated controls and treatments of varying time points should be grouped differently. In theory, the plants with higher treatment times would be expected to contain higher amounts of treatment where an untreated control should not contain any.

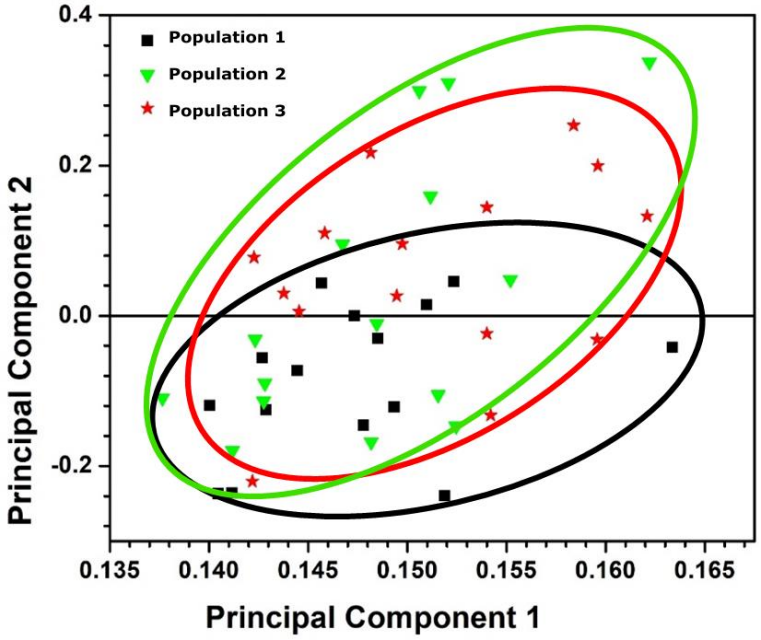

Figure 8: Principal Component Analysis (PCA) Score Plot. Data plotted from varying samples allows for visualization of both correlation and separation between data points. PCA scores are generally plotted using orthogonal principal components 1 (x-axis) and principal component 2 (y-axis). Additional principal components should be considered if needed to captured the variations in the data.

2.5 Nexus of Analytical Tools

Together, these instruments are considered, in this work, as a nexus that can be used to investigate biophysical and biochemical alterations in biological systems (figure 9). In the course of this thesis, we will investigate soft matter alterations in biological samples with respect to their morphological, mechanical, chemical and molecular shifts. The problems considered will often call for nanoscale sensitivity for better fundamental understanding of the mechanisms at the subcellular level. However, meso- and macro-scale data will be of importance to correlate small scale traits with behavior of the living system.

.

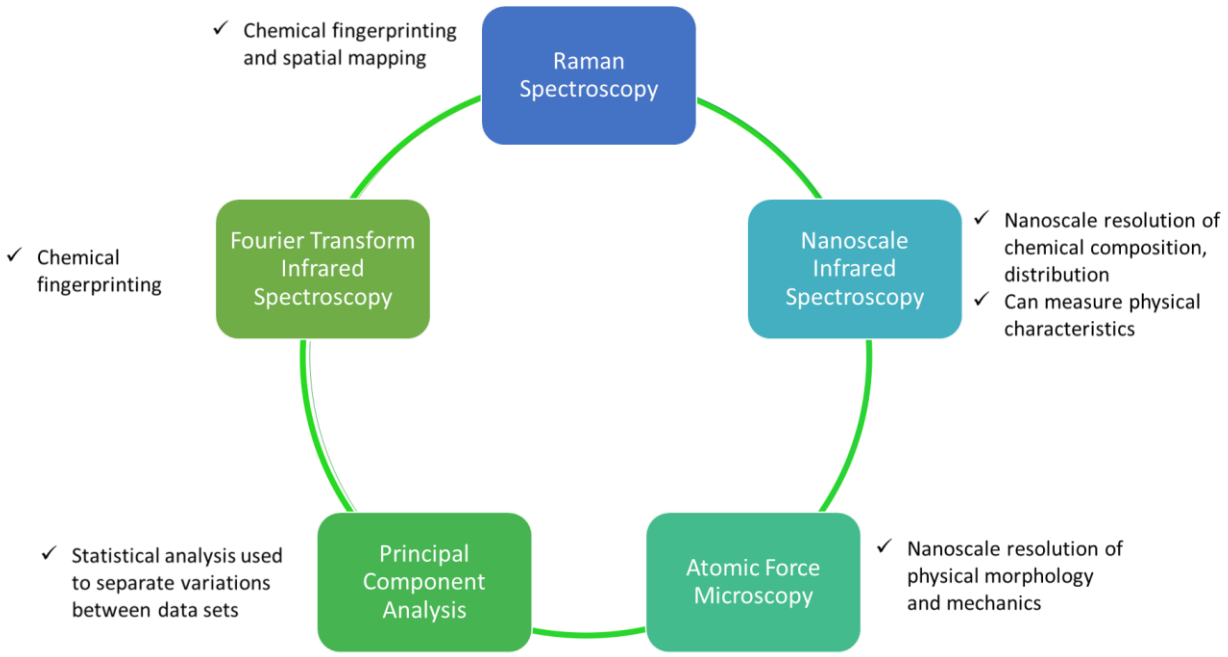

Figure 9: Nexus of Analytical Tools. Use of analytical chemical techniques such as Raman and IR spectroscopy allows for investigation of alterations occurring within a biological sample due to the vibrational modes of the materials in the systems. Mid-IR spectroscopy capture the average behavior of a large amount of material, while Raman spectroscopy offers spatial resolution mapping up too few hundred nanometers. For further details, NanoIR should be invoked. Chemical information at the nanoscale can be complemented by morphological and biomechanical traits using advanced AFM measurements. Chemometrics such as PCA allows for statistical analysis of data to separate populations based on variations making it possible to better visualize alterations occurring within samples with high background noise.

CHAPTER THREE: NANOSCALE INVESTIGATION OF CELL-EXOSOME INTERACTION

3.1 Introduction

Exosomes are nanoscale (30-100 nm) cup-shaped vesicles with a lipid bilayer membrane excreted between cells for intracellular communication (Chaput & Théry, 2011) (figure 10). They are commonly grouped with other multi-vesicular bodies (MVB), such as endosomes and liposomes, which contain membrane-bound intraluminal vesicles formed by budding into the MVB (Piper & Katzmann, 2007). Their lipid bilayers exhibit common exosome marker proteins, which have the potential for cell specific biomarkers (Bang & Thum, 2012). These entities were discovered in the 1980's (Harding, Heuser, & Stahl, 1983; Pan, Teng, Wu, Adam, & Johnstone, 1985), but have only recently gained interest from the scientific community after the discovery that exosomes can carry out RNA sequences, that can allow for the exchange of genetic information between cells and exosomes (Gibbings, Ciaudo, Erhardt, & Voinnet, 2009; Pegtel et al., 2010; Rabinowits, Gerçel-Taylor, Day, Taylor, & Kloecker, 2009; Skog et al., 2008; Valadi et al., 2007). Since then, there has been a rise in interest for characterization that would access more detailed information on exosomes. Some characteristics, such as their protein content, have been well described and since compiled into a protein database known as ExoCarta. (Mathivanan & Simpson, 2009)

The role of exosomes as antigen carriers within tumor cell lines (Raposo et al., 1996; Wolfers et al., 2001; Zheng et al., 2018), tumor metastasis inhibition (Hoshino et al., 2015), as well as promotion of immune responses (Alexander et al., 2015; Smith, Cheng, Bryant, & Schorey, 2017) is particularly intriguing. Presence of specific exosomes in pathological states, which can

be used as disease biomarkers when detected (e.g. cancer exosomes) (Saman et al., 2012; Taylor & Gercel-Taylor, 2008), have also gained attention. The idea of loading them with a treatment for a potential drug delivery vehicles (Alvarez-Erviti et al., 2011; Tianzhi Yang et al., 2015) is also of interest.

Due to the limitations in traditional analytical methods and bioassays described in previous chapters, studying single exosome-cell interactions is currently challenging. Many questions regarding the physiological mechanisms that occur during cell-exosome communication still linger. Early studies have shown fusion to plasma membrane, leading to release of exosome contents into target cells (Parolini et al., 2009; Skog et al., 2008), internalization via internal compartment fusion and eventual endocytosis/micropinocytosis (Morelli et al., 2004), phagocytosis (Morse et al., 2005), binding to cell surfaces via specific receptors (Segura, Guérin, Hogg, Amigorena, & Théry, 2007). However, these results were based on large number of exosomes. Currently, observation of single cell exosomes with target cells has not been reported. Therefore, a preliminary study in which single exosome interaction could be utilized to better understand these interactions is of great interest.

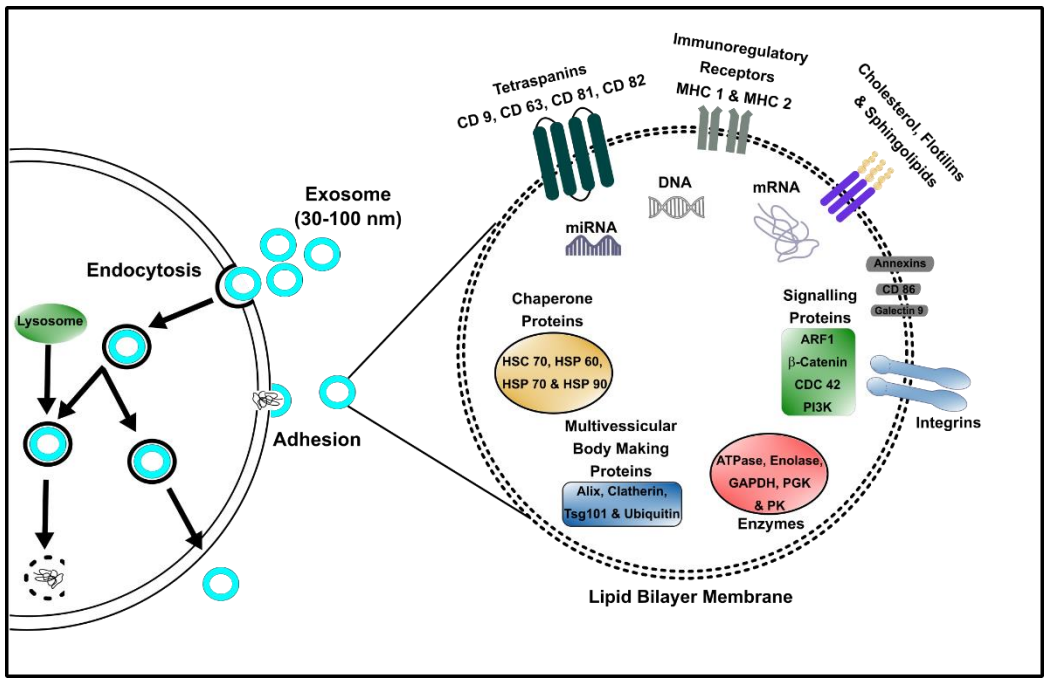

Figure 10: Exosome-Cellular Interaction and Common Components of Exosomes. Multi-vesicular bodies (MVBs) such as exosomes have several components used in cellular-exosome interaction. Exosomes have been found to interact with cells via adhesion and various forms of endocytosis. Surface components found on various exosomes such as tetraspanins, immunoregulatory receptors, lipid rafts, annexins, CD 86, galectin 9, and integrins have been found to aid in the communication and signaling between exosomes and cells. Exosomes contain information such as nucleic acids (DNA, mRNA, miRNA), signaling proteins, enzymes, chaperone proteins and MVB making proteins, which can be exchanged once exosomes interact with target cells.

Instruments capable of investigating the physical, chemical and biomechanical alterations at the nanoscale would improve the ability to answer many fundamental questions still surrounding this quickly growing field. Understanding the fundamental science behind cellular communication with extra-vesicular vehicles would make it possible to optimize the utilization of exosomes as naturally derived therapeutic options or potential disease biomarkers. NanoIR (Chapter 2 Section 2.3) allows for chemical characterization below Abbe's diffraction limit by combining infrared spectroscopy with atomic force microscopy. This study will serve as preliminary work to better

understand the biophysical and biochemical alterations which occur during interactions of HEK cells and their respective exosomes.

3.2 Materials and Methods

3.2.1 HEK 293 Cell Culture and Exosome Isolation Protocols

HEK 293 cells and HEK 293 exosome were obtained from Dr. Kiminobu Sugaya's lab group. HEK293 cells (ATCC, Manassas, VA) were cultured in Dubelcco's Modified Eagle Medium (DMEM) containing 10% exosome-depleted fetal bovine serum (FBS), laevus-glutamine (L-glutamine), and 100x nonessential amino acids in a T-75 adherent flask. The spent media was centrifuged at 10,000xg for 30 minutes to remove cell debris. Exosomes were isolated from conditioned culture media using a modified polyethylene glycol-sodium chloride (PEG-NaCl) precipitation method. 10 mL of supernatant was used to precipitate exosomes through the addition of 5 mL of 20% PEG and 200 µL of 7.5 M NaCl and subsequent overnight incubation at 4° C. The following day, the supernatant was centrifuged at 10000xg for 60 minutes and the exosome pellet was re-suspended in 1x PBS (pH 7.4, sans Calcium and Magnesium). Using cluster differentiation 63 antigen (CD63) conjugated magnetic beads, the exosomes were further purified following the manufacturer's protocol [Invitrogen by Thermo Fisher Scientific Exosome - Human CD63 Isolation/Detection (from cell culture media), Ref- 10606D].

3.2.2 Cell Immortalization and Maintenance

Human embryonic kidney (HEK 293) cells were maintained in a 5% Carbon Dioxide (CO_2) cell incubator Nu-5100E/G DH Automatic CO_2 incubator (NUAIRE Plymouth, MN) at 37 ºC. Cells were fed with cell media twice a week with HEK 293 cell media (DMEM). HEK 293 exosomes were stored at 4 ºC in 1X PBS, (pH 7.5) solution between treatments. Before treatments,

exosomes were heated to 37 ºC in a water bath before applying to HEK 293 cells at two different concentrations (100 µl & 200 µl). Once heated to 37 ºC, exosomes were introduced to HEK 293 cells at varying concentrations (100 µl & 200 µl) and incubated for 24 hours in 5% CO_2 at 37 ºC.

3.2.3 Sample Preparation

For imaging, glass slide substrates were first prepared by cleaning them using acetone, ethanol, deionized water (dH_2O), then dried with nitrogen gas. The HEK 293 cells used for investigation of biochemical shifts (FTIR & Raman spectroscopy) were removed using a cell scraper to minimize chemical alterations and future interferences during data collection. The cells removed were placed onto a glass substrate for characterization. Cells prepared for biophysical investigation were removed using (0.25%) of trypsin-Ethylenediaminetetraacetic acid (EDTA) protease (Thermo Fischer Scientific, Waltham, MA) incubated for 2 minutes to minimize structure alterations via cell removal caused by cell scrapers. For cell growth media and PBS removal, samples were centrifuged at 2000 revolutions per minute for 90 seconds. Supernatant was then removed and transferred to a clean micro-centrifuge tube and brought up to 1 mL using dH_2O. Excess PBS crystals were washed 5 µl dH_2O. This step was repeated ten times to optimize sample preparation for AFM investigation.

3.2.4 Raman Spectroscopy

Both isolated HEK 293 cells and isolated HEK 293 exosomes were characterized using Raman spectroscopy before interaction and HEK 293 cells treated with HEK 293 exosomes for 24 hours were studied. The samples were placed on glass substrates for chemical shifts investigation. The samples were investigated in ambient air with Raman spectroscopy (WiTec Alpha 300, Ulm,

Germany) using a 20x objective with a 600 g/mm grating, laser wavelength at 5 mW (1.30 a.u.) with a 2 s integration time.

3.2.5 Fourier Transmission Infrared Spectroscopy

Chemical signatures of the cells and exosomes were determined with FTIR (Perkin Elmer Spectrum 100, Waltham, MA). Exosome samples were characterized in liquid PBS. For this reason, PBS was used as background subtraction and isolate the fingerprint of exosomes. Cell growth media (DMEM) was used as the background to characterize the untreated HEK 293 cells. Resolution of the spectrometer was set to 4 cm^{-1} with standard aperture opening at 8.9 mm. An average of 3 spectra was obtained for each dataset presented here.

3.2.6 Nano-IR Measurements

The morphology and local chemical content of untreated HEK 293 and exosome-treated HEK 293 cells were measured using a NanoIR2 AFM (Anasys Instruments Santa Barbara, California). Samples were investigated for differences in both biophysical alterations, and chemical alterations in the 1530-1880 cm^{-1} range. All samples were measured in ambient air conditions. Cantilevers used were silicon end type probes coated with gold on both sides (Anasys, Santa Barbara, California). The associated resonance frequency was 11-19 kHz with a force constant of 0.1-0.6 N/m. For imaging, contact mode was selected with a scan rate of 1 Hz. Chemical maps were collected at 500 x 500 pixels at a fixed wavenumber of 1650 cm^{-1}.

3.3 Results

3.3.1 Investigating HEK 293 Cells and HEK 293 Exosomes Using Raman Spectroscopy

To understand which interactions occur between HEK cells and their exosomes, it is first important to understand the chemical structures in their native state. Components such as lipids,

nucleic acids, carbohydrates and proteins corresponds to functions of the cell such as maintaining homeostasis, maintaining cell communication with signaling proteins and binding receptors (Denzer, Kleijmeer, Heijnen, Stoorvogel, & Geuze, 2000).

Using Raman spectroscopy, the surface chemistry of the cells was found to have several peaks of interest involving lipids, proteins, and nucleic acid related components. Lipid components of the HEK cells was observed such as in 1124 cm^{-1} (C-C backbone of phospholipids) and 1452 cm^{-1} (CH Deformation). Peaks for the amino acid and protein structures associated with HEK cells range from 750 cm^{-1} (tryptophan), 1006 cm^{-1} (phenylalanine), 1264 cm^{-1} (amide III), 1310 cm^{-1} (CH deformation), 1452 cm^{-1} (CH_3 deformation), and 1663 cm^{-1} (amide I). Nucleic acid components associated at the surface of the HEK 293 cell can be visualized with peaks at 1342 cm^{-1} (adenine) and at 1584 cm^{-1} (guanine/adenine). All Raman peaks were analyzed and can be found in table 1.

Table 1: Raman Spectroscopy Peak Analysis of Isolated HEK 293 Cells.

Wavenumber (cm^{-1})	**Peak Analysis**	**Reference**
750	Tryptophan (Amino Acid)	(Huang et al., 2003)
1006	Phenylalanine (Amino Acid)	(Lin et al., 2013)
1090	Phosphate Stretch (Nucleic Acid)	(Stone et al., 2004)
1124	C-C Stretch (Lipid)	(Cheng et al., 2005)
1250	Amide III (Protein)	(Tuma, 2005)
1268	Amide III (Protein)	(Tuma, 2005)
1310	CH Deformation (Proteins)	(Lin et al., 2013)
1342	Adenine (Nucleic Acid)	(Lin et al., 2013)
1452	CH Deformation (Lipids & Proteins)	(Lin et al., 2013)
1584	Guanine (Nucleic Acid)	(Lin et al., 2013)
1663	Amide I (Protein)	(Tuma, 2005)

HEK 293 exosomes were also examined prior to interaction for surface components of interest as shown in figure 11B. Peaks associated with proteins were observed at 844 cm^{-1} (tyrosine), 1137 cm^{-1} (NH_2) and 1250 cm^{-1} & 1280 cm^{-1} (amide III peak doublet). Peaks associated

to lipid components were also abundant, including 537 cm^{-1} (cholesterol ester), 1069 cm^{-1} (C-C stretch), 1479 cm^{-1} (CH_3/CH_2 asymmetric bend). Nucleic acid components such as tyrosine were found at the peak of 1235 cm^{-1} (phosphodiester asymmetric stretch). An alcohol functional group was also observed at 581 cm^{-1} (OH bend). All Raman peaks were analyzed and can be found in table 2. Functional groups found in spectra of exosomes such as NH_2 and OH could be related to sphingosine signaling proteins which are found in various exosomes (Brouwers et al., 2013; Subra, Laulagnier, Perret, & Record, 2007; Wubbolts et al., 2003).

Table 2: Peak analysis of HEK 293 Exosomes using Raman Spectroscopy.

Wavenumber (cm^{-1})	**Peak Analysis**	**Reference**
537	Cholesterol Ester (Lipid)	(Krafft et al., 2005)
581	OH Bend (Alcohol)	(Almond et al., 2014)
844	Tyrosine (Nucleic Acid)	(Lin et al., 2013)
1069	C-C Stretch (Lipids)	(Edwards et al., 1995)
1137	NH_2	(Matthäus et al., 2008)
1235	O-P=O Asymmetric stretch (Nucleic Acid)	(Matthäus et al., 2008)
1280	Amide III (Protein)	(Lin et al., 2013)
1479	CH_3/CH_2 Asymmetric Stretch	(Matthäus et al., 2008)

Raman shifts observed in HEK 293 cells 24 hours after incubation with HEK 293 exosomes (figure 11C) can be interpreted as alterations from the unperturbed system. Shifts in regions including protein conformation shifts or interactions between the cell and exosomes. Absence of the 1280 cm^{-1} band (amide III conformation), which was observed in isolated HEK 293 cells, is also noticed after interaction with exosomes. Several additional changes were observed with disappearance of peaks associated with lipids including at 1124 cm^{-1} (C-C backbone of phospholipid) previously observed in isolated HEK 293 cells. CH peak shifted from 1452 cm^{-1} to 1432 cm^{-1} after interaction as well as absence of 2881 cm^{-1} (CH_3 stretch). Raman shifts occurring at nucleic acid associated peaks such as adenine shifting from 1342 cm^{-1} in isolated HEK 293 cells to 1333 cm^{-1} HEK 293 cells interacted with exosomes may be the result of nucleic acid information

exchange between the cell and exosomes, which has been previously observed in several other exosome-cell interactions such as mRNA and miRNA (Valadi et al., 2007). Shifts can be observed in figure 11D where untreated HEK 293 cells and HEK 293 cells 24 hours after incubation were plotted and normalized using Unscrambler software (Camo Software, Oslo, NO) to better observe chemical alterations. Further analysis via an IR spectroscopy method should be used to investigate and corroborate whether peak behaviors remain consistent for repeated cultures. A more complete peak analysis can be observed in table 3.

Table 3: Peak Analysis of Shifts Occurring Between HEK 293 Cells and Interaction of HEK 293 Exosomes 24 Hours Using Raman Spectroscopy.

Wavenumber (cm^{-1})	**Peak Analysis**	**Reference**
456	Ring Torsion of Phenyl	(Almond et al., 2014)
478	Polysaccharide (Carbohydrate)	(Shetty et al., 2006)
511	S-S Disulfide Bridge	(Cheng et al., 2005)
908	Tyrosine (Amino Acid)	(Li et al., 2011)
930	C-C Stretch (Protein)	(Lin et al., 2013)
1066	Phosphate Stretch (Nucleic Acid)	(Matthäus et al., 2008)
1100	Phosphodiester, C-N, C-C	(Matthäus et al., 2008)
1333	Adenine (Nucleic Acid) (Lin, 2013)	(Lin et al., 2013)
1453	CH Deformation (Protein)	(Matthäus et al., 2008)
1600	C=C (Lipid) Amide I (Protein)	(Lin et al., 2013)
1673	Amide I (Protein), C=C (Lipid)	(Matthäus et al., 2008)

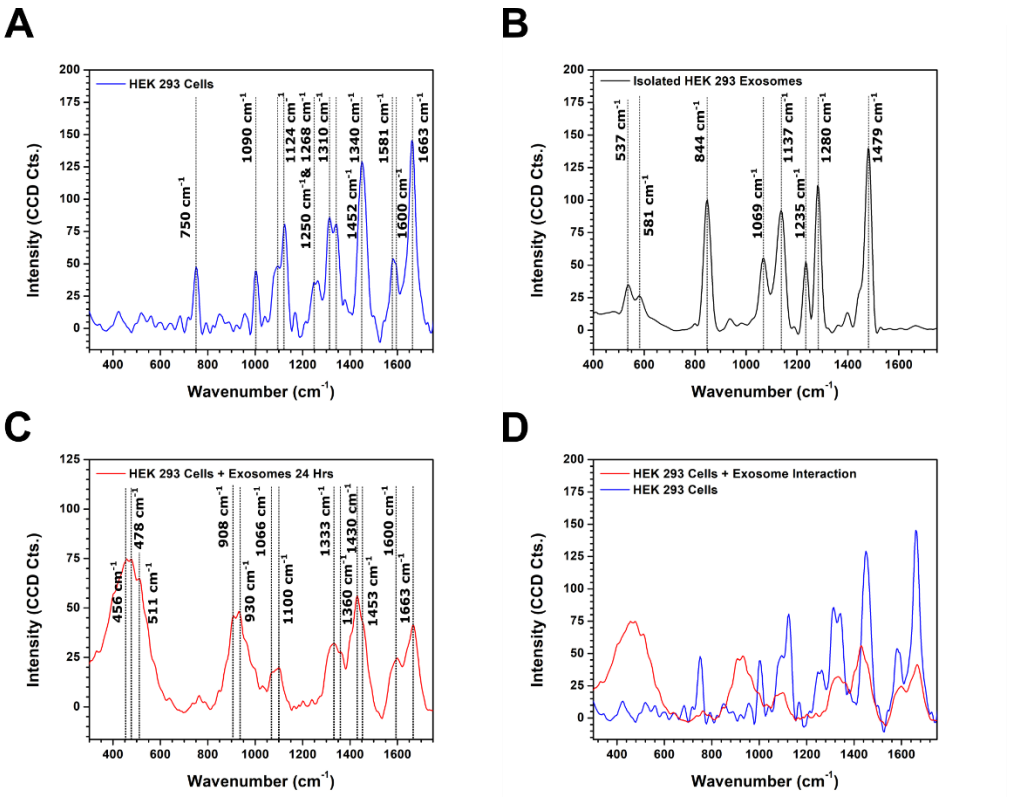

Figure 11: Analysis of Raman Spectra of Isolated HEK 293 Cells (A), Isolated HEK 293 Exosomes (B), HEK 293 Cells 24 Hours After Incubation with Exosomes (C), Comparison of HEK 293 Cell Peak Shifts (D). (A) Peaks of un-interacted HEK cells reveal several components on the cell surface including lipids such as membrane lipids (1124 cm^{-1}) and fatty acid backbones (1090 cm^{-1}), proteins such as amide I (1663 cm^{-1}) and amide III (1250 cm^{-1} & 1258 cm^{-1} peak doublet) conformations and nucleic acid components such as guanine (1584 cm^{-1}) and adenine (1342 cm^{-1}). (B) Peak analysis of isolated HEK 293 exosomes reveal several peaks regarding the lipid components (1069 cm^{-1}, 1137 cm^{-1} & 1479 cm^{-1}) as well as some protein components such as amide III (1235 cm^{-1} & 1280 cm^{-1}) conformation most likely due to signaling proteins at the surface as well as nucleic acid components such as tyrosine (844 cm^{-1}). (C) HEK 293 cells incubated with HEK 293 exosomes for 24 hours revealed several relative Raman shifts. These shifts include peak intensities for amino acids such as tyrosine. Protein changes such as disappearance of amide III peak (1250 cm^{-1}) and the presence of a band for protein backbones (930 cm^{-1}) suggests protein conformation shifts occurred during interaction. Nucleic acid shifts were observed within guanine (1584 cm^{-1} to 1333 cm^{-1}) & 1340 cm^{-1}. Lipid structures shifts were observed. (D) Overlay of normalized spectra of HEK 293 control with HEK 293 cells incubated with HEK 293 exosomes for 24 hours to observe relative Raman shifts that occurred with the interaction.

3.3.2 Investigating HEK 293 Cells and HEK 293 Exosomes Fourier Transform Infrared Spectroscopy

HEK 293 cells biochemical contents were investigated using FTIR spectroscopy before and after interaction with exosomes to determine biochemical alterations due to their interaction as a preliminary study for use during NanoIR measurements. Samples were measured in solutions of dH_2O after centrifugation to remove culture and cell debris. Due to high absorption of water, dH_2O was used in background subtraction to minimize interference. Analysis of the IR fingerprint of isolated HEK 293 cells was performed (figure 12A). Spectra reveal peaks associated with proteins such as 2973 cm^{-1} (CH_3 asymmetric stretch), 1739 cm^{-1} (fatty acid ester), 1632 cm^{-1} (amide I), 1565 cm^{-1} and (amide II). Lipid peaks were also revealed at 3000 cm^{-1} (CH Ring). Nucleic acid related peaks can be seen at 1213 cm^{-1} (Phosphate) and 1099 cm^{-1} (Phosphate). Peak analysis list is provided in table 4.

Table 4: Infrared Spectroscopy Spectra of Isolated HEK 293 Cells.

Wavenumber (cm^{-1})	**Peak Analysis**	**Reference**
3000	CH Ring	(Paluszkiewicz et al., 2001)
2973	CH_3 antisymmetric stretch (Protein)	(Matthäus et al., 2008)
1739	C=O Stretch (Lipid)	(Fabian et al., 1995)
1632	Amide I (C=O Stretch)	(Matthäus et al., 2008)
1565	Amide II (C-N Stretch)	(Matthäus et al., 2008)
1367	C-O Stretch, NH Deformation, CH Deformation	(Dovbeshko et al., 2000)
1213	Phosphate (Nucleic Acid)	(Whelan et al., 2011)
1099	Phosphate (Nucleic Acid)	(Whelan et al., 2011)

Most IR peaks found confirm findings in Raman spectra such as lipid structures, amide I and phosphate groups, all of which are common components in biological structures. IR spectra, however, revealed amide II in untreated HEK 293 cells which was not previously detectable in the Raman spectrum due to its weak intensity (Matthäus et al., 2008). Similarly amide III peak is difficult to observe in IR spectra due to its low intensity and overlapping CH_2 wagging of lipid structures (S. Cai & Singh, 2004).

Analysis of isolated HEK 293 exosomes were also performed using FTIR spectroscopy (figure 12B) to understand the components of these multi-vesicular bodies before interactions between exosomes and HEK cells. Samples were imaged in PBS solution, which due to their size (<100nm) high absorbance for water peaks occurred in the spectra. Samples were normalized with PBS spectra using Unscrambler software and PBS spectra was removed to minimize interference of investigation. Spectra on isolated exosomes reveal several peaks associated with proteins such as 3347 cm^{-1} (NH stretch), 1410 cm^{-1} (C-N stretch), 1378 cm^{-1}(C-O stretch/ NH deformation), and 1340 cm^{-1} (Amide III). These results confirm findings in Raman spectra, and are most likely associated with signaling proteins such as integrins, sphingolipids and tetraspanins found on surfaces of exosomes (Théry, Zitvogel, & Amigorena, 2002). Lipid structures were also revealed at 2970 cm^{-1} (CH3 asymmetric stretch), 2933 cm^{-1} (CH stretch), 2884 cm^{-1} (CH_3 symmetric stretch), 1466 cm^{-1} (CH deformation), and 1307 cm^{-1} (CH_2 wagging). Being a lipid bilayer vesicle, it is expected to observe several lipid peaks, but these peaks could also be associated to sphingolipids found on the surface of exosomes (Théry et al., 2002). Nucleic acid structures such as phosphate groups at 1110 cm^{-1} and 951 cm^{-1} were also observed as well as carbohydrate groups at 1129 cm^{-1}.

Table 5: Fourier Transform Infrared Spectroscopy Peak Assignment Isolated HEK 293 Exosomes**.**

Wavenumber (cm^{-1})	**Peak Analysis**	**Reference**
3347	NH Stretch (Protein)	(Eckel et al., 2001)
2970	CH_3 Asymmetric Stretch (Lipid)	(Schulz & Baranska, 2007)
2933	CH Stretch (Lipid)	(Maquelin et al., 2002)
2884	CH_3 Symmetric Stretch (Lipid)	(Schulz & Baranska, 2007)
1466	CH Deformation (Lipid)	(Maquelin et al., 2002)
1410	C-N Stretch (Protein)	(Maquelin et al., 2002)
1378	C-O Stretch, NH Deformation (Protein)	(Dovbeshko et al., 2000)
1340	Amide III (Protein)	(Chiriboga et al., 1998)
1307	CH_2 Wagging (Lipid)	(Tamm & Tatulian, 1997)
1160	C-O Stretch	(Wang et al., 1997)
1129	C-O Stretch, C-C Stretch, Ring (Carbohydrate)	(Schulz & Baranska, 2007)
1110	P-O-C Stretch (Nucleic Acid)	(Dovbeshko et al., 2000)
951	PO_4^{3-} (Nucleic Acid)	(Dovbeshko et al., 2000)
817	CH Deformation	(Movasaghi et al., 2008)

Interaction between HEK 293 cells and their exosomes (figure 12C) revealed several peak intensity shifts compared to isolated HEK 293 cells. Notable shifts not observed in Raman spectra is a shift in amide II protein band from 1565 cm^{-1} in isolated HEK cells to 1552 cm^{-1}. Another protein peak shift can be observed in amide I from 1632 cm^{-1} to 1639 cm^{-1}. These shifts are in good agreement with the results from Raman spectroscopy. Proteins alterations caused by interaction between the HEK cells and exosomes will have to be considered further. Other peak changes observed in IR spectra include nucleic acid associated shifts such as removal of phosphate

peaks (1213 cm^{-1} to 1256 cm^{-1}) and (1099 cm^{-1} to 1079 cm^{-1}). The list of assigned peaks can be observed in table 6.

Table 6: Fourier Transform Infrared Spectroscopy spectra of HEK 293 Cells 24 hours after interaction with HEK 293 Exosomes.

Wavenumber (cm^{-1})	**Peak Analysis**	**Reference**
3258	OH Stretch	(Socrates, 2001)
3064	C_2 Aromatic Stretch (Lipid)	(Schulz & Baranska, 2007)
1639	Amide I (Protein)	(Matthäus et al., 2008)
1552	Amide II (Protein)	(Matthäus et al., 2008)
1407	CH_3 Asymmetric Deformation (Proteins)	(Whelan et al., 2011)
1256	Phosphate (Nucleic Acid)	(Matthäus et al., 2008)
1079	Phosphate (Nucleic Acid)	(Wood et al., 1998)

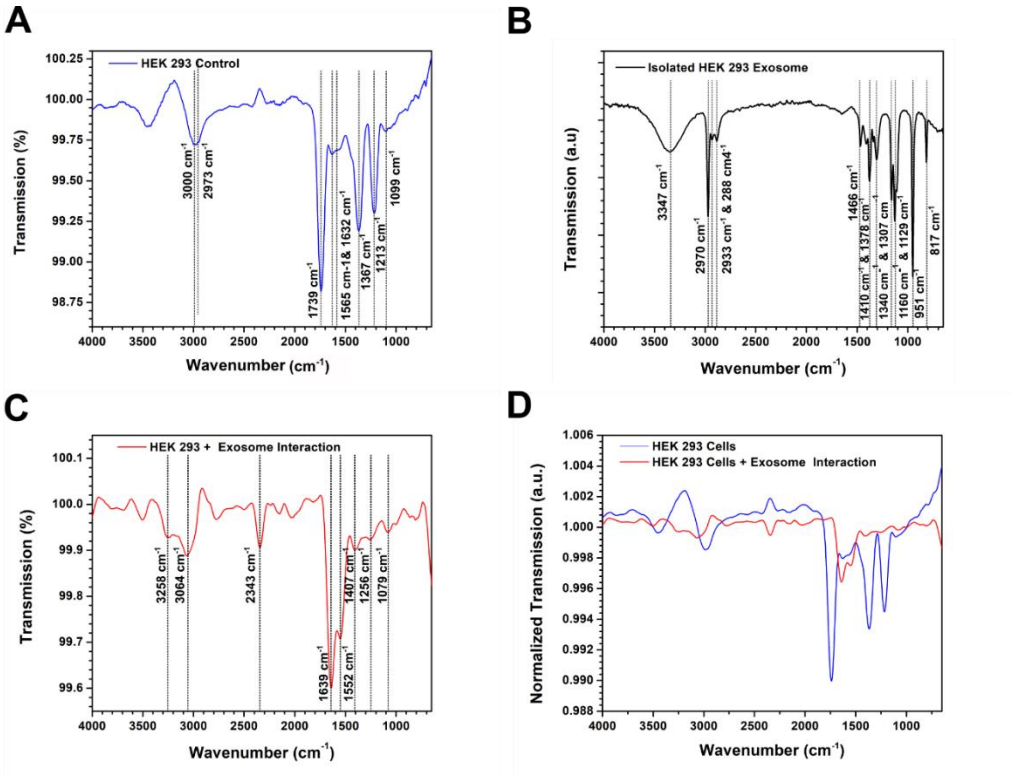

Figure 12: FTIR Spectra of Isolated HEK 293 Cells (A), Isolated HEK 293 Exosomes (B), HEK 293 Cells 24 hours After Incubation with Exosomes (C), Comparison of HEK 293 Cell Peak Shifts (D). (A) Spectra of isolated HEK 293 cells revealed proteins such as amide I (1632 cm^{-1}) and amide II (1565 cm^{-1}), nucleic acid components such as phosphate groups (1213 cm^{-1}) and (1099 cm^{-1}) as well as lipid related structures (1739 cm^{-1}). (B) Spectra of isolated HEK 293 exosomes revealed several protein peaks such as NH stretch (3339 cm^{-1}), amide III (1340 cm^{-1}), C-N (1410 cm^{-1}), and NH deformation (1378 cm^{-1}). Lipid components were observed with various CH stretching modes (2970 cm^{-1}, 2933 cm^{-1} & 2884 cm^{-1}), CH deformation (1466 cm^{-1}), and CH wagging (1307 cm^{-1}). (C) HEK 293 cells 24 hours after incubation with exosomes revealed changes in protein components such as amide I (1639 cm^{-1}), amide II (1552 cm^{-1}), CH_3 deformation, nucleic acid shifts with phosphate (1256 cm^{-1} & 1079 cm^{-1}) and C_2 aromatic stretch (3064 cm^{-1}). (D) Overlay of untreated HEK 293 cells with HEK 293 cells incubated with exosomes to better visualize shifting caused by cellular-vesicle interaction.

3.4 Discussion

Alterations of lipid, nucleic acid and protein were observed after incubation of exosomes with HEK 293 cells. Changes were observed in the FTIR and Raman spectra associated with lipid, protein and nucleic acid of the cells. Protein conformations such as amide III were found to change

as seen by the disappearance of 1250 cm^{-1} and 1268 cm^{-1} doublet observed in isolated HEK 293 cells in Raman spectroscopy. For amide II, 1565 cm^{-1} shifted to 1552 cm^{-1} in FTIR. Changes of lipid peaks in both spectra suggest disturbances to the lipid membrane associated regions could be due to interaction of exosomal signaling proteins like sphingolipids with the G coupled protein receptor sphingosine-1-phosphate receptor responsible for lipid-raft mediated endocytosis of HEK 293 cells (zu Heringdorf et al., 2001). This mechanism has been observed as an uptake pathway for dendritic cells in sphingolipid deficient HEK 293 exosomes (Izquierdo-Useros et al., 2009). Peaks associated with the lipid bilayer membrane such as CH_3, CH_2 and C=C were affected in the presence of exosomes which suggests an interaction between these 2 entities. This very preliminary investigation encourages future studies to unveil biomechanical alterations as well as nanoscale chemical alterations with instruments such as some additional instruments of the nexus.

3.5 Conclusion/Moving Forward

Raman spectroscopy and FTIR were effective methods for chemical alterations caused by interactions caused by HEK 293 cells and their exosomes. Moving forward with more sensitive with instruments capable of resolving exosomes, it may be possible to unveil single cell exosome-cell interaction properties. Further mechanisms of the exosome-cell communications should be investigated.

Our preliminary study revealed important interactions that should be addressed for more pertinent studies to be completed. Although IR and Raman shifts associated with protein, lipid, and nucleic acid components can easily be observed between 1600-800 cm^{-1}, interferance with the water signal makes it more challenging to work in liquid. Although studies have been performed to observe dried HEK cells using FTIR (Rosa, 2013), they will not be sufficient to grasp the

mechanisms taking place in living systems. Optimizing IR spectroscopy techniques with highly sensitive detection techniques in liquid would allow for more in-depth exploration of important interactions in these systems.

Interestingly, sensitive imaging have made strides in recent years and now offers an exciting future applications for probing biological samples. NanoIR is such a tool although progress is still underway. By investigating samples with tools in the nexus of analytical tools previously and in the future, a more profound knowledge of the fundamental mechanisms in naturally occurring systems is expected.

CHAPTER FOUR: NANOSCALE INVESTIGATION OF PLANT CELLS UNDER STRESS

4.1 Introduction

The nexus of tools also offers some promise regarding plant studies, particularly to investigate the nanoscale architecture of plants (Tetard et al., 2015). Such capabilities would also make it possible to investigate the nanoscale phenomena related to the physical and chemical alterations in plant systems triggered by diseases (Pérez et al., 2016), by pesticide or biocide treatment such as those with nanoparticle (Venkatachalam et al., 2017), or simply by external environments (Soliman & Tetard, 2017). By tracking biophysical and biochemical alterations, it is possible to understand alterations in the tissues as a result of treatments causing a shift at the molecular level or structural deformations caused in extreme environments, such as high temperatures (Sharma et al., 2004). Understanding these changes at the molecular level can be significant in optimizing treatment mechanisms as well as efficient chemical extractions for a variety of uses. Here we present two examples of chemical alterations of plants in which we show that high resolution spatial and spectral investigation of the tissues can have profound benefits. First, we consider an important example for disease treatment. Pathogens in plant systems such as Huanglongbing (HLB) have devastating side effects on citrus by creating biofilm plugs blocking nutrient transport. HLB has disturbed economies in several states by causing extensive crop loss or altering the taste of fruit (Paula et al., 2018), rendering them unfit for sale. Unfortunately, unlike surface bacterial infections, HLB infections thrive internally in the plant (Bové, 2006) and require treatments capable of both diffusing through natural barriers of the plant, but also be an effective antimicrobial against the disease. Instruments capable of highly sensitive detection such as FTIR and instruments capable spatial resolution such as Raman spectroscopy for confirming the pathway

of uptake of the treatment must be considered when investigating potential therapeutics. Second, we describe a novel pre-treatment method of interest in biofuel applications and biomass valorization. Biomass extraction methods can be costly due to the hardy nature of woody plants natural barriers from components such as lignin which prevent alterations from the outside environment (Cai et al., 2013). To overcome these obstacles, pre-treatments capable of breaking down cell walls and removing components responsible for natural protection must be devised in order to create a cost effective extraction method. Highly sensitive chemical detection coupled with AFM imaging capabilities make NanoIR an invaluable tool for investigating the removal of target components such as lignin while spatial resolution of Raman spectroscopy can also be utilized to confirm removal of lignin in broader regions in the cell walls such as middle lamella and secondary cell walls.

4.2 Evaluation of chemical treatments to combat plant diseases

Plant diseases can greatly affect crop productions, thereby devastating local economies dependent on crop production. If left untreated, a bacterial disease could wipe out entire crop species. Diseases such as Huanglongbing (HLB) have caused widespread bacterial epidemic due to a long asymptomatic period, coupled internal sites of infection and a highly mobile insect vector Asian citrus psyllid (ACP) (Gottwald, 2010). Antibiotics such as streptomycin have a long standing history as a prophylactic treatment against bacterial pathogens, such as bacterial pathogen *Erwinia amylovora* which causes Fireblight disease (McManus, Stockwell, Sundin, & Jones, 2002) and bacterial pathogen Xanthamonas *campestris* responsible for bacterial spot disease (Vidaver, 2002). Streptomycin is an aminoglycoside antibacterial, which binds to ribosomal pathways of bacteria, preventing protein synthesis (Stockwell & Duffy, 2012). While antibiotics

have been used to combat bacterial infections as early as the 1950's, most antibiotic applications are now used for preventative measures (Stockwell & Duffy, 2012). However, internalization of antibiotics in plants via foliar spray applications have not been investigated.

HLB in Florida is a systemic bacterial disease caused by *Candidatus* Liberibacter asiaticus (*C*Las*)* with high incidence in Florida – reports of groves with more than 95% of trees infected were reported as early as 2012 (Rouse, Irey, Gast, Boyd, & Willis, 2012). *C*Las are phloem-limited bacteria, which enter the vascular channel of citrus trees as ACPs feed from sap in the phloem (Grafton-Cardwell, Godfrey, Rogers, Childers, & Stansly, 2006). Over time, the growing bacterial colonies cause a disruption and blockage in the phloem sieve, affecting the transport of vital nutrients (Bové, 2006). Currently, there are no effective bactericides available on the market, partly due to the fact that most conventional treatments are designed to treat surface lesions and to prevent new diseases via leaves coating. In 2016, antibiotics were temporarily approved by the EPA for emergency use in an effort to reduce the losses in Florida (Putnman, 2016). However, the penetrative and therapeutic properties of the authorized antibiotics have not been fully investigated.

Here, we study antibiotics diffusion into orange leaves and their translocation throughout the plant system (leaf and stem). We will investigate the effect of adjuvant on the penetration of the antibiotic in the plant. Highly sensitive chemical detection techniques including FTIR and Raman spectroscopy are used to examine the antibiotics ability to diffuse across the plant's natural barriers upon spraying the treatment onto the leaves.

4.2.1 Materials and Methods

4.2.1.1 Materials and Concentration Calculation of Streptomycin Sulfate

Streptomycin sulfate (Fisher Scientific) was used as the model treatment to study diffusion and translocation of antibiotics across the plant membrane. In addition, Grounded® adjuvant (Helena Chemical Company) was considered due to its use in field applications as it is thought to facilitate penetration across the membrane and increase longevity of treatment against outside environments. 1% by volume adjuvant was added for aided penetration across membranes.

4.2.1.2 Seedlings

Sour orange seedlings grown in greenhouses from University of Florida-Institute of Food and Agricultural Sciences (UF-IFAS, Lake Alfred, FL) and University of Central Florida (UCF, Orlando, FL) were maintained in isolated conditions and watered with dH_2O to ensure no outside contaminants or bacterial infection would occur. All leaf samples were prepared from healthy seedlings with no major visible defects or nutrient deficiencies (zinc, boron, iron, etc.) to ensure similar parameters throughout experiment.

4.2.1.3 Seedlings treatment

200 mg/mL streptomycin treatment was used to provide significant concentrations for uptake to the seedling. 5 g of streptomycin sulfate were weighed out brought up to 50 mL with distilled water (dH_2O) in a conical tube for storage.

Control (no treatment), treatment 1 (antibiotic alone) and treatment 2 (antibiotic + adjuvant) were considered. When using adjuvant, 1% by volume (0.5 mL) of Grounded® solution was added to freshly synthesized antibiotic solution. This has been done in the hope of improving

droplet uniformity, reducing evaporation during field applications as well as improving diffusion across the stomata during spray applications of the treatment. Several treatment applications were considered for the study.

Stem Assay Uptake: For calibration of our measurements, we opted for a method of delivery using the vascular system of the leaf. In this case, the transport of the treatment is possible through the same channels as water uptake (xylem). Leaves of similar sizes were cleaved from healthy seedlings and placed in 1 mL of 200 mg/mL streptomycin sulfate solution (figure 13A) for varying durations (6 hours, 12 hours, 24 hours). After exposure, the leaves were removed from the vials and sectioned for imaging.

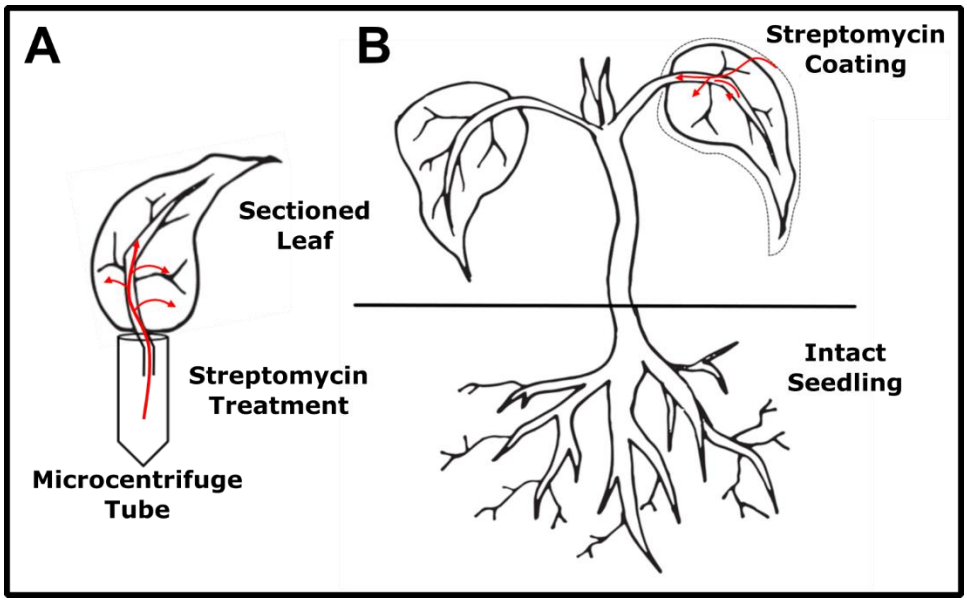

Figure 13: Stem Uptake Assay (A) and Foliar Spray Simulation (B) of Streptomycin Sulfate Treatment. Leaves were removed from healthy 6-month-old orange seedlings and placed in 1.5 mL 200 mg/mL streptomycin sulfate in a micro centrifuge tube. Uptake and propagation of treatment through the leaf can be observed at different time points. (B) 1.5 mL of 200 mg/mL streptomycin and 200 mg/mL streptomycin sulfate + 1% by volume adjuvant were placed in a sterile petri dish to coat entire surface of the leaf simulating foliar spray of treatment. Leaves remained attached to seedling during incubation time to promote natural transportation of nutrients throughout the plant and help diffuse treatment.

Foliar treatment on seedling: To model the application method used in the field, we carried out measurements on larger seedlings obtained from CREC Lake Alfred under greenhouse conditions. Leaves from healthy seedlings were dipped in 5 mL of treatment, ensuring the entire leaves, from apex to petiole, were covered (figure 13B). The leaves were maintained on the seedling for varying durations: 6 hours, 12 hours, and 24 hours. Treatment were applied between 9:30 -10:30 am to exploit stomata opening cycles (Steppe, Dzikiti, Lemeur, & Milford, 2006) to improve the chances of diffusion. Two treatments were considered: 1) 200 mg/mL streptomycin sulfate alone and 2) 200 mg/mL streptomycin sulfate with 1% by volume Grounded ® adjuvant.

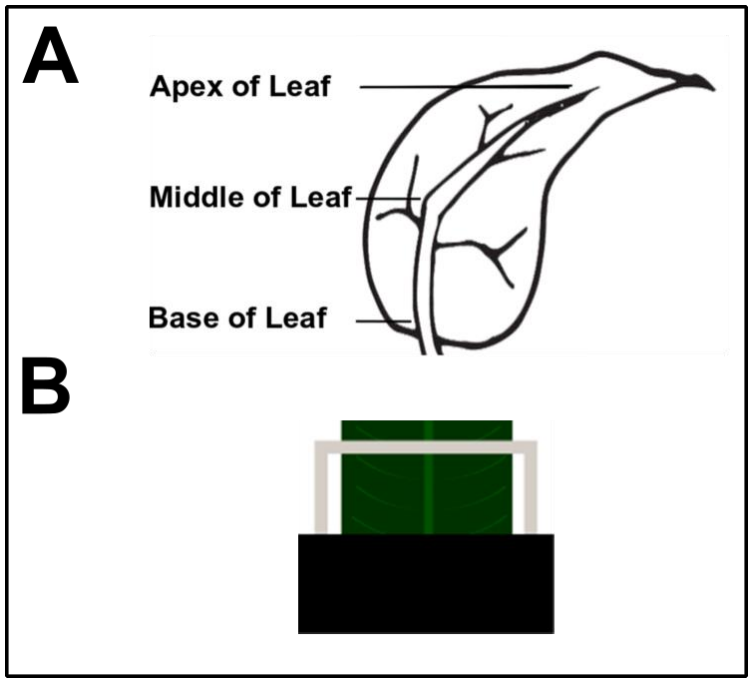

Figure 14: Leaf Sectioning (A) and Sample Holder (B). Leaves were sectioned at three regions encompassing the main areas of the plant. Sections were taken at the base of leaf, mid region of leaf and apex of leaf, placed between glass slides and held upright in a holder for Raman mapping of phloem channels in the midrib.

4.2.1.4 Tissue collection, preparation and characterization

After treatment was complete, samples were thoroughly washed with distilled water for 10 minutes and microtomed at three varying locations along the leaf (base of leaf, mid region of leaf, apex of leaf) for Raman spectroscopy (figure 14A) and placed in holders for Raman spectroscopy (figure 14B). The remaining tissues were dried in ambient air for 24 hours and ground up to a powder for Fourier transmission infrared (FTIR) spectroscopy.

4.2.1.4.1 Raman spectroscopy

Microtomed leaves were placed upright in a holding device for Raman spectroscopy on the phloem of the midrib. Raman mapping images were obtained on a confocal Raman spectroscopy (Witec Alpha 300 RA, Ulm, Germany) at 20x objective using 600 g/mm grating, excitation laser wavelength of 532 nm with a laser power of 7.636 mW and with a 1s integration time. All measurements were done under ambient conditions. Raman spectra were treated for cosmic ray removal, noise reduction using a Savitzky-Golay algorithm, and background subtraction using Witec Project Four software.

4.2.1.4.2 Fourier Transmission Infrared Spectroscopy

FTIR measurements were performed on a Spectrum 100 system (Perkin Elmer, Waltham, Ma). Resolution of the spectrometer was set to 4 cm^{-1} with standard iris aperture opening of 8.9 mm. The FTIR system is equipped with an ATR configuration previously described in chapter 2. Leaf powder was pressed down to the ATR crystal using a force of 90 (scale indicated on the software interface which was kept constant for all samples). Each sample was measured 3 times and the spectra were averaged using Origin Pro 8.5.

4.2.1.4.3 Data Analysis

Principal component analysis using Unscrambler was performed to identify potential correlation and differences between untreated and treated seedlings. For PCA completed on Raman spectroscopy, five biological replicates were obtained from three technical replicates from the base of leaves 24 hours post-treatment and for untreated samples. For analysis of FTIR data, three biological replicates were obtained from three technical replicates 24 hours post-treatment and from untreated samples.

4.2.2 Results

4.2.2.1 Tracking antibiotic uptake in the phloem using Raman spectroscopy

To study the distribution of the treatment in the plant tissue, we acquired chemical maps of the phloem in the midrib of the untreated control and treated leaves using **c**onfocal Raman spectroscopy and mapping. The spatial resolution of the confocal microscope, was adequate to pinpoint the different transport channels (e.g. xylem, phloem) of the tissues. In order to identify the characteristic peaks of the plants and to isolate the streptomycin sulfate peaks, Raman spectroscopy was used. Untreated orange seedlings revealed several peaks including CH_3 asymmetric stretch at 2940 cm^{-1}, CH_3 symmetric stretching at 2897 cm^{-1}, C=C stretching and C=O stretching at 1660 cm^{-1}, ring conjugated C=C stretch at 1620 cm^{-1}, aryl ring stretch at 1600 cm^{-1}, CH_2 bend at 1472 cm^{-1}, C-C and C-O ad 1340 cm^{-1}, O-CH_3 at 1140 cm^{-1}, and aromatic ring stretch at 1121 cm^{-1}. Complete peak analysis of plant cell walls can be found in table 7.

Table 7: Raman Spectroscopy Peak Analysis of Plant Cell Wall Components

Wavenumber (cm^{-1})	**Peak Analysis**	**Reference**
520	C-O-C Bend (Lignin)	(Gierlinger et al., 2013)
1121	Aromatic Ring Stretch (Cellulose)	(Gierlinger & Schwanninger, 2006)
1140	O-CH_3 (Cellulose)	(Sun, Simmons, & Singh, 2011)
1340	H-C-C, H-C-O Bend	(Gierlinger & Schwanninger, 2006)
1472	H-CH Bend (Lignin)	(Gierlinger et al., 2013)
1600	Aryl Ring Stretch (Lignin)	(Gierlinger et al., 2013)
1620	Ring Conjugated C=C Stretch (Lignin)	(Gierlinger & Schwanninger, 2006)
1660	C=C Stretch (Lignin), C=O Stretch (Lignin)	(Gierlinger et al., 2013)
2897	CH_3 Symmetric Stretch (Cellulose)	(Gierlinger et al., 2013)
2940	CH_3 Asymmetric Stretch (Lignin)	(Agarwal et al., 2011)

Investigation of streptomycin sulfate with Raman spectroscopy to optimize treatment tracking based on peaks shadowed by peaks naturally occurring in plants (figure 15A). Raman spectra revealed peaks at 407 cm^{-1} (C-N, C-OH, CH_3), 444 cm^{-1} (N-C-S), 531 cm^{-1} (C-O deformation), 586 cm^{-1} (OH bend), 609 cm^{-1} (CH deformation), 846 cm^{-1} (C-O-C, 985 cm^{-1} (S=O), 1080 cm^{-1} (C-N), 1120 cm^{-1} (NH_2), 1360 cm^{-1} (CH_3 scissoring), 1460 cm^{-1} (CH_2/CH_3 deformation), 2910 cm^{-1} (CH_3 stretch), 2940 cm^{-1} (CH_2 stretch). Based on investigation of untreated seedlings, S=O at 985 cm^{-1} was the best method since it is the only peak not competing with a naturally occurring peak from citrus seedlings. P assignments of streptomycin sulfate can be found in appendix A.

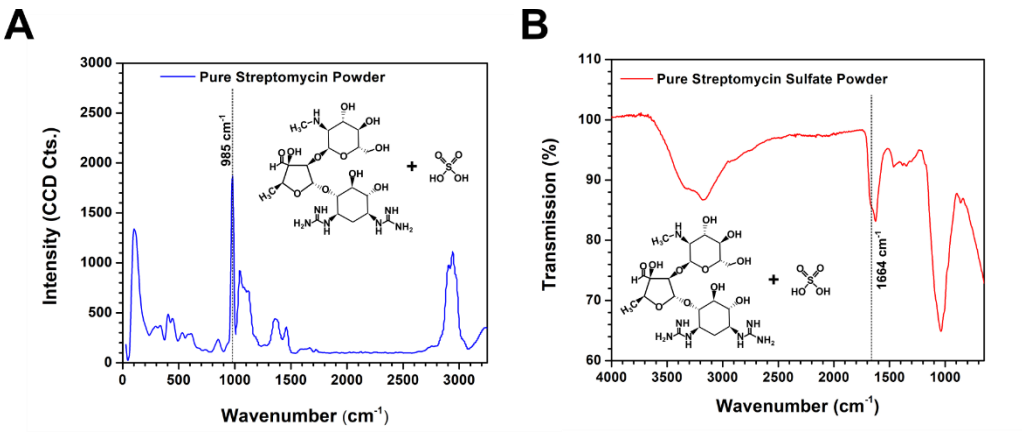

Figure 15: Raman (A) and FTIR Spectra (B) of Pure Streptomycin Sulfate. IR spectra of pure streptomycin sulfate powder reveals major peaks such as 1664 cm^{-1} (amide I). Raman spectra of pure streptomycin sulfate reveal several peaks of interest, however only one peak, 985 cm^{-1} (S=O) remains cleanly observable by naturally occurring plant peaks. These peaks will be used to track treatment uptake in orange seedlings based off lack of naturally competing peaks from orange seedlings.

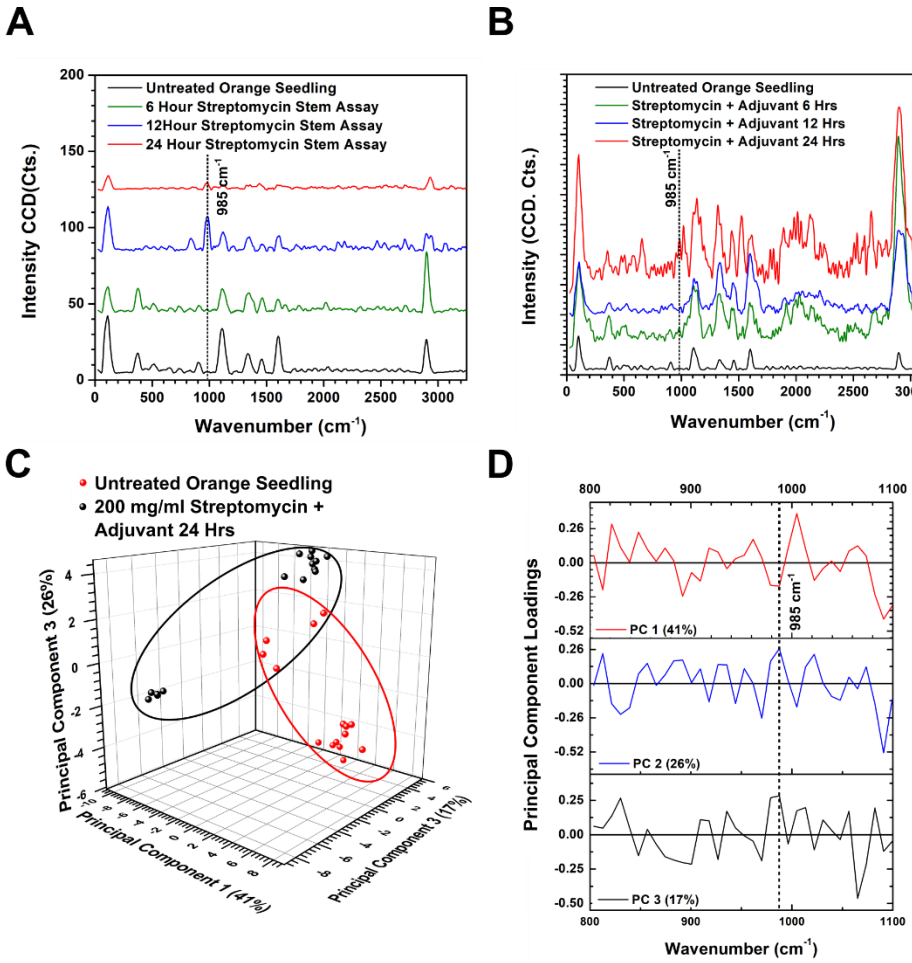

Figure 16: Raman Spectra of Untreated and Antibiotic Treated Orange Seedlings. A) Raman spectra of stem uptake assays at base of the leaf: Sectioned leaves treated with 200 mg/ml streptomycin sulfate for varying time points (0,6,12,24 hours). Treatment can be tracked with 985 cm^{-1}. Antibiotic uptake can be observed as soon as 6 hours after treatment. 24 hours after treatment, antibiotic was found in all regions of the midrib. B) Raman spectra for foliar spray application of 200 mg/ml streptomycin sulfate and 1% by vol adjuvant sectioned at base of the leaf. Uptake of treatment can be tracked at 985 cm^{-1}. Treatment can be observed as early as 24 hours with full translocation of leaves being observed at 24 hours post treatment. C) Principal component analysis scores plotting of untreated orange seedlings and 200 mg/ml streptomycin sulfate + 1% by volume Grounded adjuvant treated with foliar spray application. Visible variation occurs between treated and untreated samples along PC 1 (41%), PC 2 (26%), and PC 3 (17%). D) Loadings of PC 1 shows negative correlation of peak at 985 cm^{-1} (S=O) while PC 2 and PC 3 show positive correlation to 985 cm^{-1}.

A stem uptake assay was completed at varying time points (0,6,12,24 hours) as a baseline uptake model by exploiting transport pathways of antibiotics in plants previously reported in

literature (Herklotz, Gurung, Heuvel, & Kinney, 2010; Kong et al., 2007). Results of stem uptake assay revealed uptake of streptomycin sulfate based on sulfate bond (985 cm^{-1}) as early as 6 hours of treatment at the base of the leaf (figure 16A). Uptake in all three sectioned regions (figure 14A) was observed at 24 hours after treatment (not pictured). For foliar spray application, seedlings were treated with 200 mg/ml with 1% by volume adjuvant added with the seedlings still attached to the plant to promote natural transport of nutrients throughout the leaves. Seedlings were treated between 9:00am and 10:00 am ET to optimize maximum stomatal opening cycles and sap flow cycles previously reported (Steppe et al., 2006). Results for foliar spray application show uptake of antibiotic based on 985 cm^{-1} (S=O) occurred around 24 hours post treatment (figure 16B). However, treatment was observed in all three regions sectioned at 24 hours (not pictured). These findings may support the idea that the adjuvant is capable of increasing the time and efficiency of antibiotics ability to penetrate the leaf membrane and exploit additional stomata opening oscillations.

4.2.2.1.1 Principal component analysis of uptake with Raman spectroscopy

Principal component analysis of an untreated orange seedling and orange seedlings treated with a foliar spray application of 200 mg/ml streptomycin sulfate with 1% by volume added Grounded ®) adjuvant. Since Raman spectroscopy of plants exhibit fluorescence and noise within the spectra, PCA of the spectra was cut to a range of 800 cm^{-1} to 1100 cm^{-1} to reduce outside factors from being compiled into the variation. Results showed a large amount of variation between PC 1 (41%), PC 2 (26%), PC 3 (17%) and PC 4 (10%). Scores of untreated orange seedling and seedlings treated with 200 mg/ml streptomycin sulfate with adjuvant were plotted against PC 1 and PC 2 (figure 16 C). These scores reveal a large amount of variation occurring across PC 1 and

PC 2. Loadings of PC's 1 and 2 were then plotted to determine where the variation was occurring in accordance to the spectra (figure 16D). PC 2 and PC 3 loadings revealed a presence of a peak at 985 cm^{-1} while PC 1 did not exhibit a peak in that region. PC1 does not exhibit a clean sign of treatment signature, hence further investigations will be required to identify the nature of the variation.

4.2.2.2 Tracking antibiotic uptake using infrared spectroscopy

Untreated seedlings were treated as a baseline to understanding cellular components to better optimize treatment tracking using FTIR (figure 17A). IR spectra revealed peaks associated with plant components such as cellulose, hemicellulose, lignin, pectin, xylan, and proteins. Cellulose related peaks were observed at 1370 cm^{-1} (CH_3 bend) and 1058 cm^{-1} (C-O-C stretch) and 1025 cm^{-1} (C-O-C). Hemicellulose associated peaks were revealed at 2920 cm^{-1} (CH_2), 1632 cm^{-1} (OH), 1156 cm^{-1} (C-O-C), and 1025 cm^{-1} (C-O-C). Lignin associated peaks at 2920 cm^{-1} (CH_2 stretch), 1726 cm^{-1} (C=O stretch), and 1246 cm^{-1} (C-O). Other components such as pectin was observed at 1417 cm^{-1} ($C\text{-}O\text{-}O^-$) and 1100 cm^{-1} (C-OH). Xylan was observed at 1246 cm^{-1} (syringyl ring), and proteins were being observed at 3339 cm^{-1} (NH) and 1521 cm^{-1} (C=N). Peak assignment of untreated citrus seedlings is provided in table 8.

Table 8: Fourier Transform Infrared Spectroscopy Peak Analysis of Orange Seedling Components.

Wavenumber (cm^{-1})	**Peak Analysis**	**Reference**
3339	NH (Amide A)	(Dovbeshko et al., 2000)
2920	CH_2 (Hemicellulose/Lignin)	(Emmanuel et al., 2015)
2853	CH Bend	(Sene et al., 1994)
1726	C=O Stretch (Lignin)	(Emmanuel et al., 2015)
1632	H-OH (Hemicellulose)	(Emmanuel et al., 2015)
1521	C=N (Amide II)	(Sene et al., 1994)
1417	C-O-O- Stretch (Pectin)	(Schulz & Baranska, 2007)
1370	CH_3 Bend (Cellulose)	(Emmanuel et al., 2015)
1246	C-O (Lignin), Syringyl Ring (Xylan)	(Faix et al., 1991)
1156	C-O-C (Cellulose/Hemicellulose)	(Ferraz et al., 2000)
1100	C-OH Bend (Pectin)	(Kacurakova et al., 2000)
1058	C-O-C (Cellulose)	(Kacurakova et al., 2000)
1025	C-O-C (Cellulose/Hemicellulose)	(Emmanuel et al., 2015)

Spectra were then acquired for the pure solutions of antibiotics using FTIR are presented in figure 17B. FTIR spectra of streptomycin sulfate powder revealed bands peaks such as 3350 cm^{-1} (OH, CH, and NH), 3167 cm^{-1} (NH symmetric stretch), 1664 cm^{-1} (C=O) 1626 (OH), 1462 cm^{-1} (CH deformation), 1381 cm^{-1} (CO stretch), 1348 cm^{-1} (N=CH), 1037 cm^{-1} (SO_4^{2-}), and 861 cm^{-1} (SO_4^{2-}). In IR spectroscopy, 1664 cm^{-1}, which is indicative of an amide I bond, can be used to investigate uptake of treatment using FTIR. Streptomycin sulfate's bands at1037 cm^{-1} cannot be readily distinguished from orange seedlings bands at 1025cm^{-1} and 1058 cm^{-1} peaks as well streptomycin's band at 3167 cm^{-1} peak is largely overshadowed by orange seedlings broad NH bond peak ranging from 3339 cm^{-1}. Therefore, amide I (1664 cm^{-1}) in IR spectra can be used to verify streptomycin presence within seedlings, indicating antibiotic migration into treated leaves. IR band assignment of FTIR spectra for streptomycin sulfate can be found in appendix B.

Building on previous results observed with Raman spectroscopy, FTIR was used to investigate uptake of 200 mg/ml streptomycin sulfate with 1% by volume Grounded ® adjuvant. Results showed a shoulder peak at 1664 cm^{-1} associated to amide I (C=O) 24 treatment (figure 15B) which was previously observed in IR spectra of pure streptomycin sulfate (figure 15B). This peak is in accordance to the findings in the Raman spectroscopy investigation of streptomycin sulfate uptake. Since the band at 1664 cm-1 corresponds to a functional group that represents the antibiotic molecule, the uptake of streptomycin can be confirmed. This is in contrast with Raman, where only sulphate ions could be tracked.

4.2.2.2.1 Principal component analysis of uptake in IR spectra

Due to interference with naturally occurring hemicellulose 1632 cm^{-1} peak as well as other antibiotic associated peaks, principal component analysis was performed to better investigate uptake. PCA score plots showed variation across PC 1 (81%), as well as variation occurring across PC 2 (12%) (figure 20C). Loadings of PC 1 and PC 2 were plotted to reveal where the variation between the components. Loadings for PC 1 revealed a positive shift at 1664 cm^{-1}, indicative of the amide I peak present in streptomycin sulfate with a negative correlation in PC 2. However, there is no strong association due to the noise of components such as lignin and hemicellulose caused greater variation than the treatment. Further analysis using other chemometrics such as partial least square regression may better determine separation of components.

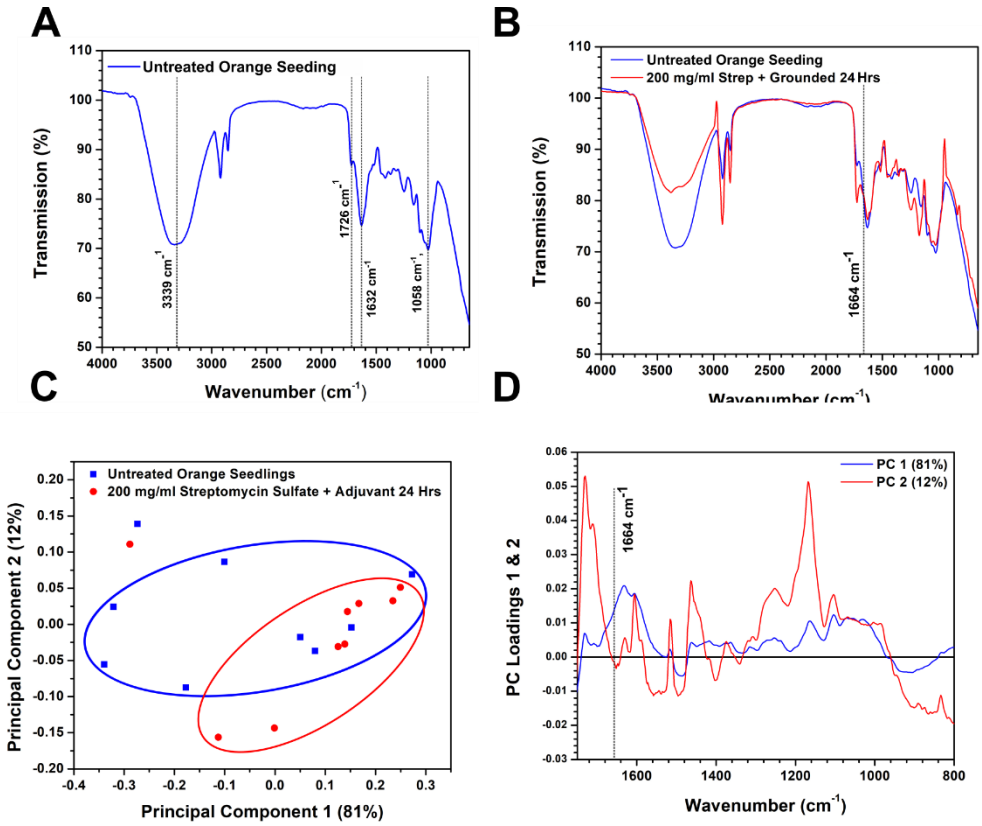

Figure 17: Fourier Transform Infrared Spectroscopy and Principal Component Analysis of Treated and Untreated Orange Seedlings. (A) FTIR spectra of sour orange seedlings, naturally occurring peaks at 3339 cm^{-1} and 1058 cm^{-1} overlap peaks associated with treatment. Amide I peak at 1664 cm^{-1} should be present between peaks at 1726 cm^{-1} and 1632 cm^{-1} representative of the seedling (B) Orange Seedlings treated for 24 hours with 200 mg/mL streptomycin sulfate + 1% by volume Grounded ® adjuvant. Results show uptake which can be visualized by shoulder of 1632 cm^{-1} peak revealing 1664 cm^{-1} peak associated with amide I. (C) PCA score can be used to better visualize differences across PC 1 (81%) and PC 2 (12%) of treated and untreated seedlings. (D Loadings show positive correlation at 1664 cm^{-1} in PC 1 with negative correlation in PC 2.

4.2.3 Discussion

Foliar spray application was found to diffuse across the leaf membrane's natural barriers and was even found to translocate throughout the entire treated leaf in 24 hours with the aid of fatty acid adjuvants using both FTIR and Raman spectroscopy as well as confirmation through PCA to confirm results. FTIR was capable of tracking structural components confirming uptake of antibiotic in the plant while the spatial resolution of Raman spectroscopy made it possible to characterize uptake of treatment in the plant's transport channels locally. The presence of streptomycin in phloem transport channels confirmed the role of these channels in treatment transportation, as well as a treatment opportunity against phloem specific diseases. Literature suggests antibiotics become inert due to ultraviolet light exposure within one week of application (Stockwell & Duffy, 2012) which should reduce risk of unwanted introduction of antibiotics into the environment. Overall our findings with baseline assay are in agreement with previous reports regarding antibiotic uptake via root systems (Herklotz et al., 2010) as well as through manure treated soil samples (Bassil, Bashour, Sleiman, & Abou-Jawdeh, 2013; Boxall et al., 2006; Dolliver, Kumar, & Gupta, 2007; Kumar, Gupta, Baidoo, Chander, & Rosen, 2005). For economic reasons, it is not likely that treatments will be repeated more often than once daily, therefore with 24 hours allowing for movement of the treatment, it creates a possible protocol for effective treatment.

4.3 Evaluation of chemical treatments to produce biofuel

Besides their importance for food production, plants are also a great source of biomass for biofuel production. With traditional non-renewable energy sources depleting, there has never been a better time to investigate alternative fuel options from renewable sources. Alternative fuel

sources from lignocellulosic feedstock's have been gaining momentum as a biofuel source due to the processing potential of biomass processes potential for combustion, fermentation, pyrolysis (Gordobil, Moriana, Zhang, Labidi, & Sevastyanova, 2016; Kim, Lee, & Park, 2016; Monlau et al., 2013). Nevertheless, the most attractive feature of plants, may be their enormous level of bioavailability. However, extraction of lignin and cellulose has proven to be a daunting task due to lignin's evolution to be the natural line of defense against outside environments, including chemical alterations – a phenomenon called *recalcitrance* (Ruiz-Dueñas & Martínez, 2009). Without efficient cellulose extraction methods, cellulose based biofuels remain too costly to be considered profitable for mass production which is needed to transition towards biofuels. As of 2015, the estimate fuel price for cellulose derived biofuels averaged $10/gal (Brown, 2015) due to low production and inability to compete with petroleum. There are several avenues that can be considered to improve the estimate fuel price. In particular, here we will focus on deconstruction and valorization of the biomass waste materials. For deconstruction, A new thermochemical deconstruction co-solvent, tetrahydrofuran (THF):dH_2O (1:1) was proposed due to its ability to promote lignin extraction necessary for efficient biomass removal in previous studies (C. M. Cai et al., 2013). By augmenting the hydrolysis, THF:dH_2O has the ability to depolymerize lignin causing cell wall decomposition and making cellulose more readily available for extraction. However, the effect of the treatment on the structural and chemical properties of the plant cell wall is not well understood. Here, we investigate the deconstructive capabilities of THF:dH_2O on eastern cottonwood (Populus deltoides), more commonly known as poplar. We illustrate how nanoscale chemical imaging can boost the understanding of plant tissues nanoscale properties to provide information on deconstruction mechanisms and efficiency.

4.3.1 Materials and Methods

4.3.1.1 Biomass Deconstruction

Samples of eastern cotton wood (Populus deltoides) were obtained from Oak Ridge National Laboratory for the chemical deconstruction and investigation of lignin extraction. An equivolume of THF: dH_2O was the co-solvent used to for the lignin removal pretreatment. 1% by weight sulfuric acid was also used in additional studies to investigate complete removal of lignin. Samples were placed in a homemade reaction chamber (Fig. 18) and insulated with blocks to maintain constant temperature during reaction.

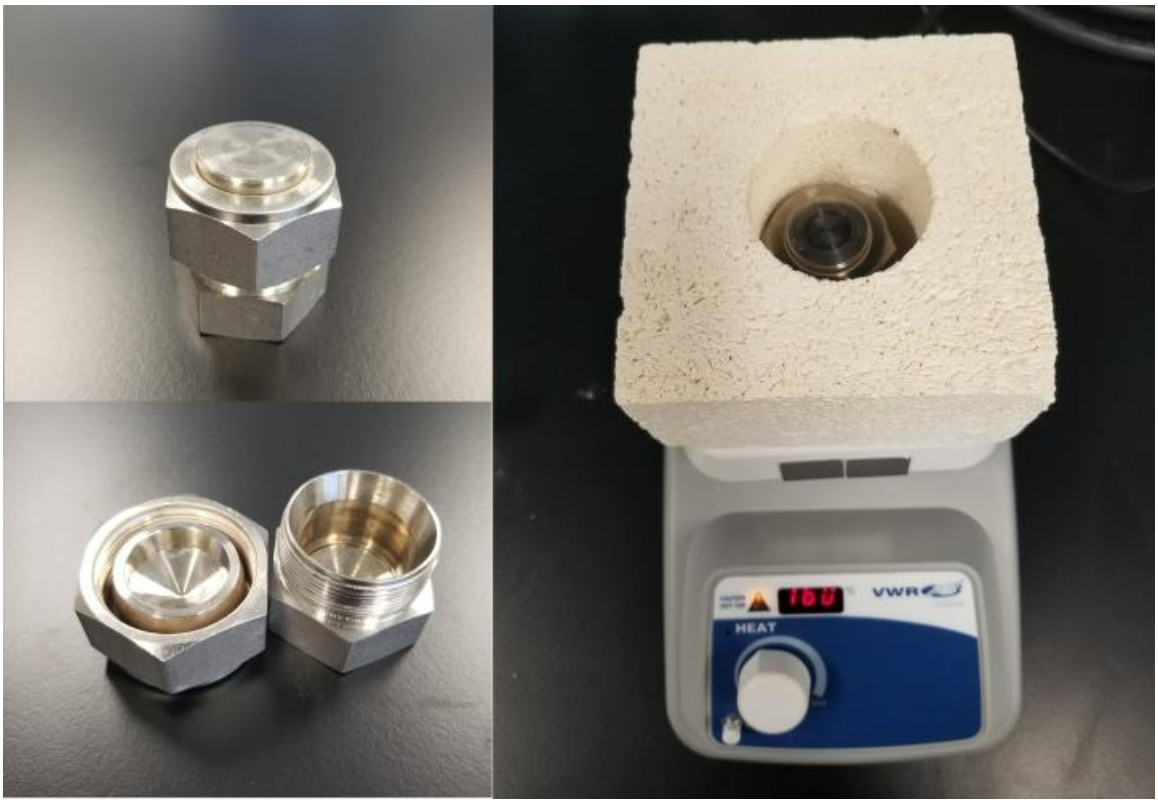

Figure 18: Co-Solvent Heating Chamber and Insulating Bricks. THF: dH_2O co-solvent was placed in chamber with poplar sections and sealed before reaction. Insulating bricks were placed around and on top of reaction chamber on hot plate to maintain constant temperature.

4.3.1.2 Concentration of Tetrahydrofuran: Water and Sulfuric Acid

Tetrahydrofuran (THF) was diluted to a 1:1 ratio of THF: dH_2O in lab for chemical deconstruction of poplar cell walls. Concentrated sulfuric acid (H_2SO_4) was obtained from Sigma Aldrich (St. Louis, MO) and diluted to 0.1 M for additional investigation of cellular deconstruction in additional experiments.

4.3.1.3 Sample Sectioning and Chemical Heating Techniques

Thin sections (<1mm) of poplar were obtained using 9-gauge razor blades to ensure high surface area interaction of co-solvent with cell walls of the poplar. Several thinly sliced samples were then added with 2 mL of a 1:1 ratio of THF: dH_2O to a small reaction chamber and heated to 160 ºC using a hotplate (VWR Radnor, PA) covered with thermal insulation. Samples were maintained at 160 ºC for varying time points (30 minutes, 60 minutes). In additional experiments, 10% by volume of H_2SO_4 was added to 2 mL 1:1 ratio of THF: dH_2O for investigation of additional cell wall destruction for lignin extraction. Sections were then removed from the reactor, and rinsed, before being placed on glass slides to dry in preparation for nanoscale investigation of cell wall structure and remaining chemical components.

4.3.1.4 Subcellular Decomposition Investigated with Raman Spectroscopy

Composition of the plant cell walls was investigated with a confocal Raman microscope (WiTec Alpha 300 RA) using a 20x objective a 532 nm wavelength and 600 g/mm grating. Laser power was set to 5.104 mW scanning samples with a 1 second integration time. Inelastic scattered light was then detected using charge coupled device (CCD) in -60 ºC.

4.3.1.5 Morphological and Biochemical Alterations Investigated with NanoIR

Poplar cross sections were analyzed using NanoIR (Anasys, Santa Barbara, California) before and after chemical treatments for sensitive detection of chemical composition as well as structural changes. Atomic force microscopy (AFM) was used to investigate the morphological alterations of treated poplar and NanoIR was used to investigate chemical signatures in the 1530cm^{-1} to 1800cm^{-1} range, with a 2cm^{-1} step. NanoIR measurements were carried out following a protocol in literature (Dazzi & Prater, 2016). Au-coated cantilevers (PR-EX-nIR2 k~0.07 N/m) were used for contact mode imaging and NanoIR mode.

4.3.2 Results

Raman imaging of untreated poplar revealed several lignin associated peaks such as 530 cm^{-1} (O-CH_3 deformation), 1052 cm^{-1} (C-O of aryl–O–CH_3), 1472 cm^{-1} (CH_2 bend) 1600 cm^{-1} (aryl ring stretch), 1620 cm^{-1} (ring conjugated C=C), 1660 cm^{-1} (C=C stretch, C=O stretch) and 2940 cm^{-1} (CH_3 asymmetric stretch) all of which make it possible to track the removal of lignin after the co-solvent reaction (figure 19A). Complete analysis of these peaks, which are similar to the peaks found in orange seedlings, are found in table 9.

Removal of lignin can be observed as early as 15 minutes with intensity shifts at 1660 cm^{-1} and 2940 cm^{-1} (figure 19B). Significant reduction of lignin can be observed by significantly lower intensities of all lignin associated peaks (figure 19C). Spectra of 60-minute treatment revealed complete removal of lignin associated peaks across the spectra (figure 19D). As reaction time increased, fluorescence of the spectra was also observed to increase, which is indicative of lignin removal and reposition due to lignin's naturally fluorescent nature. Reactions with THF: dH_2O and 1% weight sulfuric acid added were also used to investigate complete removal of lignin to

avoid settling on plant cell wall after investigation. The sulfuric acid created too high of a fluorescence to produce observable spectra.

Table 9: Raman spectra of Populus Deltoides Cross Section.

Wavenumber (cm^{-1})	**Peak Analysis**	**Reference**
530	O-CH_3 Deformation (Lignin)	(Sun, Simmons, & Singh, 2011)
1052	C-O of aryl–O–CH_3 (Lignin)	(Gierlinger & Schwanninger, 2006)
1121	Aromatic Ring Stretch (Cellulose)	(Gierlinger & Schwanninger, 2006)
1140	O-C-H_3 (Cellulose)	(Sun, Simmons, & Singh, 2011)
1340	H-C-C, H-C-O Bend	(Gierlinger & Schwanninger, 2006)
1472	H-C-H Bend (Lignin)	(Gierlinger et al., 2013)
1600	Aryl Ring Stretch (Lignin)	(Gierlinger et al., 2013)
1620	Ring Conjugated C=C Stretch (Lignin)	(Gierlinger & Schwanninger, 2006)
1660	C=C Stretch (Lignin), C=O Stretch (Lignin)	(Gierlinger et al., 2013)
2897	C-H_3 Symmetric Stretch (Cellulose)	(Gierlinger et al., 2013)
2940	C-H_3 Asymmetric Stretch (Lignin)	(Agarwal et al., 2011)

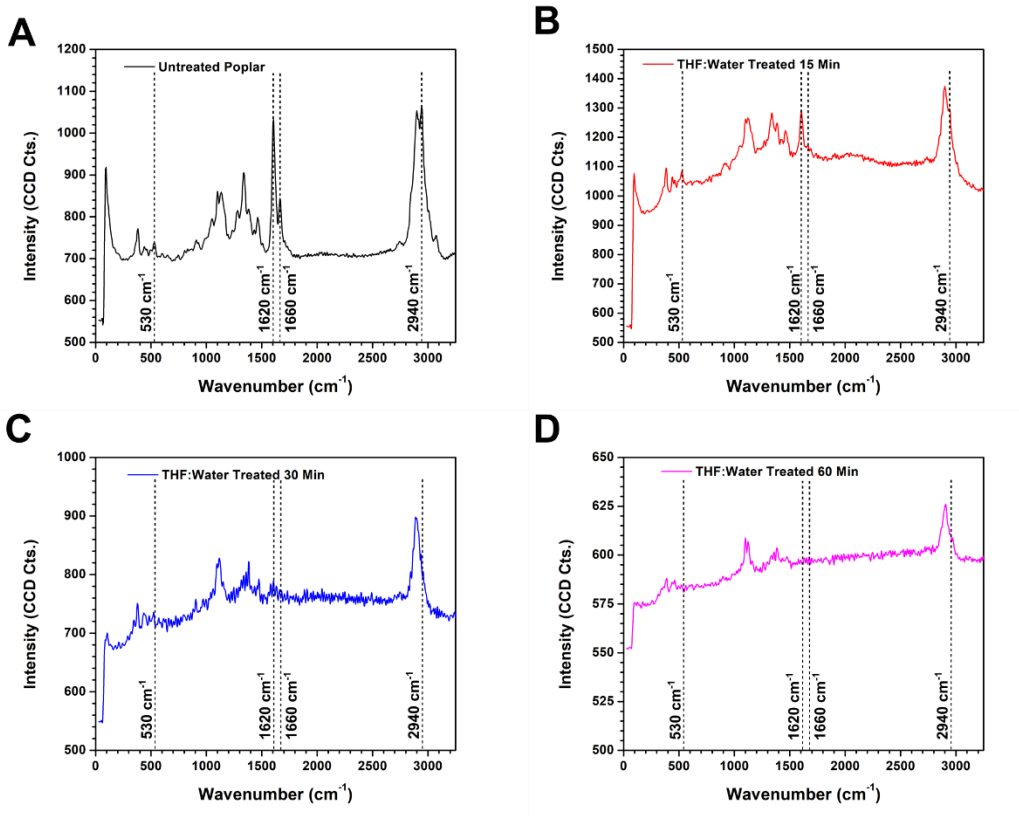

Figure 19: Raman Spectra of THF: Water Co-Solvent Treated Poplar Sections. A) Raman spectra of untreated eastern cotton wood poplar (*Populus deltoides*). Lignin, the plant's natural defense against foreign alterations, reveals peaks at 1620 cm^{-1}, 1660 cm^{-1}, and 2940 cm^{-1} which will be observed for determination of lignin removal post co-solvent treatments based on absence or presence in Raman spectra. B) Raman spectra of poplar after being treated with 1:1 ratio of THF:dH_2O co-solvent at 160 ºC for 15 minutes. Spectra reveals lignin to be removed, although not completely, based on the relative intensity shifts between lignin and non-lignin peaks when compared to untreated poplar spectra (A). C) Raman spectra of poplar after being treated with 1:1 ratio of THF:dH_2O co-solvent at 160 ºC for 30 minutes. Spectra reveals significant lignin removal based on noticeably lower peaks at the 1620 cm^{-1}-1660 cm^{-1} range as well as diminished 2940 cm^{-1} shoulder peak. Although significant amounts of lignin removal can be observed, there are still minor peaks at both 1620 cm^{-1} and 1660 cm^{-1} suggesting total removal of lignin from cell wall had not occurred. D) Raman spectra of poplar after being treated with 1:1 ratio of THF:dH_2O co-solvent at 160 ºC for 60 minutes. Spectra shows total absence of lignin signatures in all three noted peaks (1620 cm^{-1}, 1660 cm^{-1}, 2940 cm^{-1}). Total absence of all three peaks suggests total lignin removal from cell wall was achieved.

The change in Raman bands and the fluorescence background suggests a release of lignin.

To understand the localized distribution of lignin and cellulose across the plant cell walls, we

explored the tissues further with NanoIR. At each wavelength the position and intensity of the cantilever contact resonance was recorded to form an 'absorption vs. wavenumber' spectrum. When the laser wavelength coincides with an absorption band of the material, the amplitude measured is large. Cell wall deconstruction was confirmed by investigating presence of lignin (1650 cm^{-1}) with nanoscale infrared spectroscopy. Samples measured within the region of 1530 cm^{-1}-1880 cm^{-1} with a tuned laser fixed at 1650 cm^{-1}. Peaks associated with IR spectra in this range can be seen in table 10.

Table 10: Infrared Spectra Between 1530 cm^{-1}-1810 cm^{-1} of Populus Deltoides Cross Section.

Wavenumber (cm^{-1})	**Peak Analysis**	**Reference**
1720	C=C Stretch (Lignin)	(Emmanuel et al., 2015)
1670	C=O Stretch (Lignin)	(Emmanuel et al., 2015)
1598	Ring Conjugated C=C Stretch (Lignin)	(Emmanuel et al., 2015)
1596	C-O Stretch (Cellulose)	(Pandey & Pitman, 2003)
1595	Symmetric Aryl Ring Stretch (Lignin)	(Pandey & Pitman, 2003)

AFM topographical images were obtained for both untreated and co-solvent treated poplar (figure 20A, 20B) revealing cell wall deconstruction post treatment. IR spectra were then obtained to investigate chemical alterations complementary to morphological shifts after co-solvent treatment. Infrared spectra of local cell wall structures such as middle lamella and secondary cell walls were investigated. Middle lamella is responsible for the adhesion between neighboring cell walls, providing additional support to the plant structure. Secondary cell walls are generally more rigid to provide structural confidence within a plant system. Due to presence of lignin in these structures, the cells become less permeable to water and external factors as well as losing flexibility, compared to primary cell wall features. These spectra obtained at the different locations show related signatures of lignin bands of both secondary cell wall and middle lamella with a

signature around 1650 cm^{-1} (figure 20C). Poplar treated with co-solvent reveal significant reduction of lignin presence in both cell wall structures (figure 20D) in the 1610 cm^{-1}-1720 cm^{-1} range. Another noteworthy intensity shift occurs at 1595 cm^{-1}, indicative of substantial aromatic bond formation. The formation of an aromatic ring is coupled with peaks diminishing in a 1720 cm^{-1}-1610 cm^{-1} coupled with broadening shift at 1730 cm^{-1}.

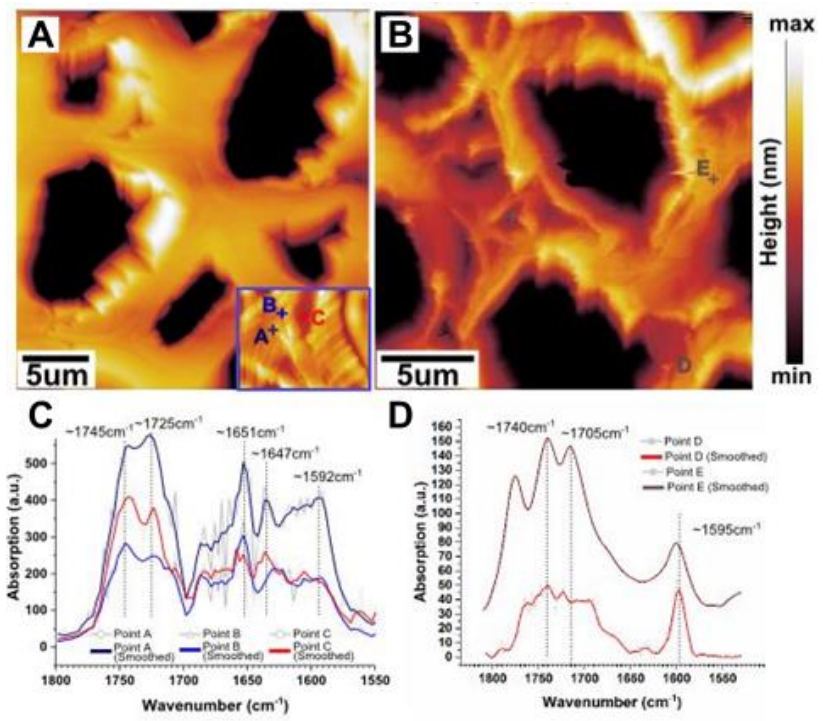

Figure 20: Nanoscale Investigation of Morphological and Chemical Alterations with NanoIR. NanoIR was used to investigate the removal of lignin post co-solvent treatment with nanoscale resolution. A) Atomic force microscopy (AFM) topography images of untreated eastern cotton wood poplar (*Populous deltoides*) cross section. B) AFM topography image of co-solvent reacted cell wall environment revealing noticeable deconstruction to cell wall formation. C) IR spectra of untreated poplar across regions of cell wall including middle lamella (points A, B) and secondary cell wall structure (point C). D) IR spectra (point D) of sample treated in co-solvent for 60 minutes, exhibiting significant decreases of lignin presence in cell walls, confirming alterations observed in reacted cell wall topography (B).

Co-solvent THF: dH_2O was confirmed as an effective method for lignin extraction out of cell walls of lignin rich sources such as hardwood poplars. With peaks associated with lignin shifted and cell wall deformation, it is possible to extract cellulose with ample efficiency, which could drive down the cost for feedstock biofuel productions. NanoIR was able to confirm shift in peaks associated with lignin from naturally lignin-rich regions such as the secondary cell walls, with both AFM topographic images showing striking morphological changes in cell wall structures

complemented by the IR spectra showing withdrawal of lignin from the cell via disappearance of lignin associate peaks (1647cm^{-1}, 1651 cm^{-1}, 1725 cm^{-1} on the infrared wavelength).

Removal of lignin peaks was also observed with Raman spectra with disappearance of associated lignin peaks (1620 cm^{-1}, 1660 cm^{-1}, 2940 cm^{-1} within Raman wavelength). The removal of lignin associated ring conjugated C=C peaks of coniferyl/sinapyl alcohol and C=O stretch of coniferaldehyde/sinapalaldehyde suggests rearrangement of polymers located within cell wall structures. The data revealing time dependent amounts of lignin removal can allow for specific amounts of removal, allowing to finely tune cellulose/lignin ratios to optimize for specific biofuel/biomass needs.

4.3.3 Discussion

THF: dH_2O proved to be an effective co-solvent for the removal of lignin as a pretreatment for efficient cellulose extraction. Raman spectroscopy and NanoIR provided pinpoint accuracy to investigate subcellular components of the plant cell walls to determine which areas of cells are most affected by reaction. The investigation of removal of lignin determined that an hour long pretreatment may be necessary with just a 1:1 ratio of THF: dH_2O, but can be adjusted to remove specific quantities of lignin based off reaction duration. Addition of small quantities of sulfuric acid made it possible to cut down on reaction time which can be proven to more efficient, cutting back on time and costs of pre-treatment.

4.4 Conclusion

Raman spectroscopy and IR spectroscopy were able to provide complementary information in the investigation of antibiotic uptake in plants. Using Raman spectroscopy, it was possible to probe site specific channels of the plant such as the phloem to ensure uptake of antibiotic was

being detected in the right region. Raman, however, was only able to detect the sulfate ion, so investigation with another instrument was necessary. FTIR was capable of tracking uptake of streptomycin based off the amide I group of streptomycin, but was not capable of the high spatial resolution of Raman spectroscopy. With both of these instruments, it was possible to track the uptake of treatment with propagation of antibiotic across the entire leaf when adjuvant was used, which was capable of matching the diffusion efficacy of the stem uptake assay model. Now that it is confirmed the diffusion of antibiotics across leaf surfaces into internal cellular components, future studies should investigate movement across the entire plant system with a focus on accumulation in fruits of these plants to assure accidental ingestion does not occur.

The nexus of analytical tools creates highly sensitive investigational techniques capable of pushing the bounds of what is possible. By fully encompassing these techniques, a new method of antibiotic application has been explored to more capably use these treatments in emergency situations. It was also possible to obtain nanoscale biochemical and morphological alterations were observed for optimizing the biomass extraction process. This information could be critical for the advancement and efficiency and valorization of biofuel extraction techniques promoting alternative fuels as a very real possibility as a primary fuel source in the future.

CHAPTER FIVE: CONCLUSION

High resolution instruments with the ability to measure down to a few nanometers allows for ultrafine definition of morphological features, however these instruments often lack the ability to measure critical components such as chemical fingerprints, as well as, regularly require the environment to be in vacuum. These requirements can be detrimental to biological samples because they are sensitive to environmental changes such as temperature and oxygen deprivation, but also because they are dynamic and can be easily contaminated by bacteria, requiring special precautions and additional environmental constraints. Therefore, utilizing instruments with nanoscale capabilities is of ultimate importance. With the recent advancements in instrumentation, such as ultrafast Raman spectroscopy, chemical and physical characterization can now be conducted at a fraction of the time of their more traditional Raman counterparts (D'Arco, Ferrara, Indolfi, Tufano, & Sirleto, 2017). Here, our studies show the implications of applying a novel multisystem approach comprised of advanced nanoscale instruments, such as AFM, Raman spectroscopy, FTIR, and NanoIR to study biological soft matter.

Overall, the results from our studies illustrate that nanoscale investigation can reveal new information regarding the properties of biological interfaces, both for plant and human tissues. To explore these levels, we implemented the nexus of systems to probe the chemical and physical properties of these interfaces, from the micrometer to nanometer scales. We first demonstrated the ability to use Raman spectroscopy, FTIR, and NanoIR spectroscopy to investigate biochemical shifts that occur when HEK 293 cells interact with exosomes for potential therapeutic applications. We postulated that we would be able to identify HEK 293 exosome uptake by HEK 293 cells by observing biochemical shifts. We determined that these exosomes were taken up by the cells and

were able to further deduce the mode of uptake to endocytosis, eliminating other methods such as surface adherence.

We also sought to further demonstrate additional applications in biological soft matter that this nexus could be applied to. Outside of human cell biology, we applied our system to plant cell biology to study the uptake and translocation of antibiotics. The ability of drugs to penetrate hard to reach regions, such as the phloem, is of significant interest to researchers seeking to answer how to treat many bacterial plant based diseases plaguing the agricultural sector. Therefore, we utilized Raman spectroscopy, FTIR, and NanoIR to again follow chemical changes establishing the uptake and movement throughout the leaf. Lastly, we pushed the nexus to answer real world questions regarding renewable resources to understand chemical and physical changes occurring during plant processing for alternative fuels and biomass production. Consequently, these techniques assisted in identifying the chemical and physical shifts that occur as the lignin is removed plant cell walls.

APPENDIX A: RAMAN SPECTRA OF PURE STREPTOMYCIN SULFATE POWDER

Table 11: Raman Spectra of Pure Streptomycin Sulfate Powder

Wavenumber (cm^{-1})	**Peak Analysis**	**Reference**
407	C-N, C-OH, CH_3	(Socrates, 2001)
444	N-C-S	(Farquharson et al., 2005)
531	C-O Deformation	(Socrates, 2001)
586	OH Bend	(Almond et al., 2014)
609	CH Deformation	(Socrates, 2001)
846	C-O-C	(Shetty et al., 2006)
985	S=O	(Socrates, 2001)
1040	C-O Stretch	(Schulz & Baranska, 2007)
1080	C-N Stretch	(Socrates, 2001)
1120	C-N Stretch	(Nawaz et al., 2011)
1360	CH_3 Scissoring	(Socrates, 2001)
1460	CH_2/CH_3 Deformation	(Cheng et al., 2005)
2910	CH_3 Stretch	(Quintás et al., 2004)
2940	CH_2 Stretch	(Schulz & Baranska, 2007)

APPENDIX B: FTIR SPECTRA OF PURE STREPTOMYCIN SULFATE

Table 12: FTIR Spectra of Pure Streptomycin Sulfate Powder.

Wavenumber (cm^{-1})	**Peak Analysis**	**Reference**
3350	OH, NH, CH	(Caspers et al., 2001)
3167	NH Symmetric Stretch	(Dovbeshko et al., 2000)
1664	C=O (Amide I)	(Matthäus et al., 2008)
1626	OH	(Socrates, 2001)
1462	CH Deformation	(Maquelin et al., 2002)
1381	C-O Stretch	(Socrates, 2001)
1348	N-CH	(Socrates, 2001)
1037	SO_4^{2-}	(Socrates, 2001)
861	S-OH	(Socrates, 2001)

REFERENCES

Abbe, E. (1874). A contribution to the theory of the microscope and the nature of microscopic vision. *Proc. Bristol Nat. Soc, 1*, 200-261.

Adatia, M., & Besford, R. (1986). The effects of silicon on cucumber plants grown in recirculating nutrient solution. *Annals of Botany, 58*(3), 343-351.

Agarwal, U. P. (2006). Raman imaging to investigate ultrastructure and composition of plant cell walls: distribution of lignin and cellulose in black spruce wood (Picea mariana). *Planta, 224*(5), 1141.

Agarwal, U. P., McSweeny, J. D., & Ralph, S. A. (2011). FT–Raman investigation of milled-wood lignins: softwood, hardwood, and chemically modified black spruce lignins. *Journal of wood Chemistry and technology, 31*(4), 324-344.

Alcaraz, J., Buscemi, L., Grabulosa, M., Trepat, X., Fabry, B., Farré, R., & Navajas, D. (2003). Microrheology of human lung epithelial cells measured by atomic force microscopy. *Biophysical journal, 84*(3), 2071-2079.

Alexander, M., Hu, R., Runtsch, M. C., Kagele, D. A., Mosbruger, T. L., Tolmachova, T., . . . O'Connell, R. M. (2015). Exosome-delivered microRNAs modulate the inflammatory response to endotoxin. *Nature communications, 6*, 7321.

Almond, L. M., Hutchings, J., Lloyd, G., Barr, H., Shepherd, N., Day, J., . . . Stone, N. (2014). Endoscopic Raman spectroscopy enables objective diagnosis of dysplasia in Barrett's esophagus. *Gastrointestinal endoscopy, 79*(1), 37-45.

Alvarez-Erviti, L., Seow, Y., Yin, H., Betts, C., Lakhal, S., & Wood, M. J. (2011). Delivery of siRNA to the mouse brain by systemic injection of targeted exosomes. *Nature biotechnology, 29*(4), 341.

Anderson, N., Anger, P., Hartschuh, A., & Novotny, L. (2006). Subsurface Raman imaging with nanoscale resolution. *Nano letters, 6*(4), 744-749.

Bang, C., & Thum, T. (2012). Exosomes: new players in cell–cell communication. *The international journal of biochemistry & cell biology, 44*(11), 2060-2064.

Barnes, J., Tian, L., Loftis, J., Hiznay, J., Comhair, S., Lauer, M., & Dweik, R. (2016). Isolation and analysis of sugar nucleotides using solid phase extraction and fluorophore assisted carbohydrate electrophoresis. *MethodsX, 3*, 251-260.

Barth, A. (2007). Infrared spectroscopy of proteins. *Biochimica et Biophysica Acta (BBA)-Bioenergetics, 1767*(9), 1073-1101.

Bassil, R. J., Bashour, I. I., Sleiman, F. T., & Abou-Jawdeh, Y. A. (2013). Antibiotic uptake by plants from manure-amended soils. *Journal of Environmental Science and Health, Part B, 48*(7), 570-574.

Benıtez, J. J., Matas, A. J., & Heredia, A. (2004). Molecular characterization of the plant biopolyester cutin by AFM and spectroscopic techniques. *Journal of Structural Biology, 147*(2), 179-184.

Binnig, G., Quate, C. F., & Gerber, C. (1986). Atomic force microscope. *Physical review letters, 56*(9), 930.

Binnig, G., Rohrer, H., Gerber, C., & Weibel, E. (1982). Tunneling through a controllable vacuum gap. *Applied Physics Letters, 40*(2), 178-180.

Bové, J. M. (2006). Huanglongbing: a destructive, newly-emerging, century-old disease of citrus. *Journal of plant pathology*, 7-37.

Boxall, A. B., Johnson, P., Smith, E. J., Sinclair, C. J., Stutt, E., & Levy, L. S. (2006). Uptake of veterinary medicines from soils into plants. *Journal of Agricultural and Food Chemistry, 54*(6), 2288-2297.

Boyle, W. S., & Smith, G. E. (1970). Charge coupled semiconductor devices. *Bell Labs Technical Journal, 49*(4), 587-593.

Bro, R., & Smilde, A. K. (2014). Principal component analysis. *Analytical Methods, 6*(9), 2812-2831.

Brouwers, J. F., Aalberts, M., Jansen, J. W., van Niel, G., Wauben, M. H., Stout, T. A., . . . Stoorvogel, W. (2013). Distinct lipid compositions of two types of human prostasomes. *Proteomics, 13*(10-11), 1660-1666.

Brown, T. R. (2015). A techno-economic review of thermochemical cellulosic biofuel pathways. *Bioresource technology, 178*, 166-176.

Brunk, U. T., Dalen, H., Roberg, K., & Hellquist, H. B. (1997). Photo-oxidative disruption of lysosomal membranes causes apoptosis of cultured human fibroblasts. *Free Radical Biology and Medicine, 23*(4), 616-626.

Brunner, C., Niendorf, A., & Käs, J. A. (2009). Passive and active single-cell biomechanics: a new perspective in cancer diagnosis. *Soft Matter, 5*(11), 2171-2178.

Cai, C. M., Zhang, T., Kumar, R., & Wyman, C. E. (2013). THF co-solvent enhances hydrocarbon fuel precursor yields from lignocellulosic biomass. *Green Chemistry, 15*(11), 3140-3145.

Cai, S., & Singh, B. R. (2004). A distinct utility of the amide III infrared band for secondary structure estimation of aqueous protein solutions using partial least squares methods. *Biochemistry, 43*(9), 2541-2549.

Caspers, P. J., Bruining, H. A., Puppels, G. J., Lucassen, G. W., & Carter, E. A. (2001). In vivo confocal Raman microspectroscopy of the skin: noninvasive determination of molecular concentration profiles. *Journal of investigative dermatology, 116*(3), 434-442.

Chaput, N., & Théry, C. (2011). *Exosomes: immune properties and potential clinical implementations.* Paper presented at the Seminars in immunopathology.

Cheng, W. T., Liu, M. T., Liu, H. N., & Lin, S. Y. (2005). Micro-Raman spectroscopy used to identify and grade human skin pilomatrixoma. *Microscopy research and technique, 68*(2), 75-79.

Chevillet, J. R., Kang, Q., Ruf, I. K., Briggs, H. A., Vojtech, L. N., Hughes, S. M., . . . Gallichotte, E. N. (2014). Quantitative and stoichiometric analysis of the microRNA content of exosomes. *Proceedings of the National Academy of Sciences, 111*(41), 14888-14893.

Chiriboga, L., Xie, P., Yee, H., Vigorita, V., Zarou, D., Zakim, D., & Diem, M. (1998). Infrared spectroscopy of human tissue. I. Differentiation and maturation of epithelial cells in the human cervix. *Biospectroscopy, 4*(1), 47-53.

Chundawat, S. P., Donohoe, B. S., da Costa Sousa, L., Elder, T., Agarwal, U. P., Lu, F., . . . Dale, B. E. (2011). Multi-scale visualization and characterization of lignocellulosic plant cell wall deconstruction during thermochemical pretreatment. *Energy & Environmental Science, 4*(3), 973-984.

Cooper, D. (2002). *Valence bond theory* (Vol. 10): Elsevier.

Costa, K. D. (2004). Single-cell elastography: probing for disease with the atomic force microscope. *Disease markers, 19*(2, 3), 139-154.

Croset, A., Delafosse, L., Gaudry, J.-P., Arod, C., Glez, L., Losberger, C., . . . Vilbois, F. (2012). Differences in the glycosylation of recombinant proteins expressed in HEK and CHO cells. *Journal of biotechnology, 161*(3), 336-348.

Cross, S. E., Jin, Y.-S., Rao, J., & Gimzewski, J. K. (2007). Nanomechanical analysis of cells from cancer patients. *Nature nanotechnology, 2*(12), 780.

Cuerrier, C. M., Lebel, R., & Grandbois, M. (2007). Single cell transfection using plasmid decorated AFM probes. *Biochemical and biophysical research communications, 355*(3), 632-636.

D'Arco, A., Ferrara, M. A., Indolfi, M., Tufano, V., & Sirleto, L. (2017). Label-free imaging of small lipid droplets by femtosecond-stimulated Raman scattering microscopy. *Journal of Nonlinear Optical Physics & Materials*, 1750052.

Dazzi, A., & Prater, C. B. (2016). AFM-IR: technology and applications in nanoscale infrared spectroscopy and chemical imaging. *Chemical reviews, 117*(7), 5146-5173.

Dazzi, A., Prazeres, R., Glotin, F., & Ortega, J. (2005). Local infrared microspectroscopy with subwavelength spatial resolution with an atomic force microscope tip used as a photothermal sensor. *Optics letters, 30*(18), 2388-2390.

Denzer, K., Kleijmeer, M. J., Heijnen, H., Stoorvogel, W., & Geuze, H. J. (2000). Exosome: from internal vesicle of the multivesicular body to intercellular signaling device. *Journal of cell science, 113*(19), 3365-3374.

Diaspro, A. (2001). Confocal and two-photon microscopy: foundations, applications and advances. *Confocal and Two-Photon Microscopy: Foundations, Applications and Advances, by Alberto Diaspro (Editor), pp. 576. ISBN 0-471-40920-0. Wiley-VCH, November 2001.*, 576.

Dolliver, H., Kumar, K., & Gupta, S. (2007). Sulfamethazine uptake by plants from manure-amended soil. *Journal of environmental quality, 36*(4), 1224-1230.

Dovbeshko, G. I., Gridina, N. Y., Kruglova, E. B., & Pashchuk, O. P. (2000). FTIR spectroscopy studies of nucleic acid damage. *Talanta, 53*(1), 233-246.

Eckel, R., Huo, H., Guan, H.-W., Hu, X., Che, X., & Huang, W.-D. (2001). Characteristic infrared spectroscopic patterns in the protein bands of human breast cancer tissue. *Vibrational Spectroscopy, 27*(2), 165-173.

Edwards, H. G., Farwell, D. W., Williams, A. C., Barry, B. W., & Rull, F. (1995). Novel spectroscopic deconvolution procedure for complex biological systems: vibrational components in the FT-Raman spectra of ice-man and contemporary skin. *Journal of the Chemical Society, Faraday Transactions, 91*(21), 3883-3887.

Eliasson, C., Claybourn, M., & Matousek, P. (2007). Deep subsurface Raman spectroscopy of turbid media by a defocused collection system. *Applied spectroscopy, 61*(10), 1123-1127.

Emmanuel, V., Odile, B., & Céline, R. (2015). FTIR spectroscopy of woods: A new approach to study the weathering of the carving face of a sculpture. *Spectrochimica Acta Part A: Molecular and Biomolecular Spectroscopy, 136*, 1255-1259.

Fabian, H., Jackson, M., Murphy, L., Watson, P. H., Fichtner, I., & Mantsch, H. H. (1995). A comparative infrared spectroscopic study of human breast tumors and breast tumor cell xenografts. *Biospectroscopy, 1*(1), 37-45.

Fahrenfort, J. (1961). Attenuated total reflection: A new principle for the production of useful infra-red reflection spectra of organic compounds. *Spectrochimica Acta, 17*(7), 698-709.

Faria, E. C., Ma, N., Gazi, E., Gardner, P., Brown, M., Clarke, N. W., & Snook, R. D. (2008). Measurement of elastic properties of prostate cancer cells using AFM. *Analyst, 133*(11), 1498-1500.

Farquharson, S., Shende, C., Inscore, F. E., Maksymiuk, P., & Gift, A. (2005). Analysis of 5-fluorouracil in saliva using surface-enhanced Raman spectroscopy. *Journal of Raman Spectroscopy, 36*(3), 208-212.

Ferraro, J. R. (2003). *Introductory raman spectroscopy*: Academic press.

Frick, U. B., & Schaller, A. (2002). cDNA microarray analysis of fusicoccin-induced changes in gene expression in tomato plants. *Planta, 216*(1), 83-94.

Gibbings, D. J., Ciaudo, C., Erhardt, M., & Voinnet, O. (2009). Multivesicular bodies associate with components of miRNA effector complexes and modulate miRNA activity. *Nature cell biology, 11*(9), 1143.

Gierlinger, N., Keplinger, T., Harrington, M., & Schwanninger, M. (2013). Raman imaging of lignocellulosic feedstock. In *Cellulose-Biomass Conversion*: InTech.

Gierlinger, N., & Schwanninger, M. (2006). Chemical imaging of poplar wood cell walls by confocal Raman microscopy. *Plant physiology, 140*(4), 1246-1254.

Gordobil, O., Moriana, R., Zhang, L., Labidi, J., & Sevastyanova, O. (2016). Assesment of technical lignins for uses in biofuels and biomaterials: Structure-related properties, proximate analysis and chemical modification. *Industrial crops and products, 83*, 155-165.

Gottwald, T. R. (2010). Current epidemiological understanding of citrus huanglongbing. *Annual review of phytopathology, 48*, 119-139.

Goubet, F., Jackson, P., Deery, M. J., & Dupree, P. (2002). Polysaccharide analysis using carbohydrate gel electrophoresis: a method to study plant cell wall polysaccharides and polysaccharide hydrolases. *Analytical biochemistry, 300*(1), 53-68.

Grafton-Cardwell, E. E., Godfrey, K. E., Rogers, M. E., Childers, C. C., & Stansly, P. A. (2006). Asian citrus psyllid.

Graham, D., Stevenson, R., Thompson, D. G., Barrett, L., Dalton, C., & Faulds, K. (2011). Combining functionalised nanoparticles and SERS for the detection of DNA relating to disease. *Faraday discussions, 149*(1), 291-299.

Hackett, L. P., Li, W., Ameen, A., Goddard, L. L., & Liu, G. L. (2018). Plasmonic Metal-Insulator-Metal Capped Polymer Nanopillars for SERS Analysis of Protein-Protein Interactions. *The Journal of Physical Chemistry C*.

Hamley, I. W. (2013). *Introduction to soft matter: synthetic and biological self-assembling materials*: John Wiley & Sons.

Hanlon, E., Manoharan, R., Koo, T. W., Shafer, K., Motz, J., Fitzmaurice, M., . . . Feld, M. (2000). Prospects for in vivo Raman spectroscopy. *Physics in Medicine & Biology, 45*(2), R1.

Harding, C., Heuser, J., & Stahl, P. (1983). Receptor-mediated endocytosis of transferrin and recycling of the transferrin receptor in rat reticulocytes. *The Journal of cell biology, 97*(2), 329-339.

Henderson, R. (1995). The potential and limitations of neutrons, electrons and X-rays for atomic resolution microscopy of unstained biological molecules. *Quarterly reviews of biophysics, 28*(2), 171-193.

Herklotz, P. A., Gurung, P., Heuvel, B. V., & Kinney, C. A. (2010). Uptake of human pharmaceuticals by plants grown under hydroponic conditions. *Chemosphere, 78*(11), 1416-1421.

Hori, R., & Sugiyama, J. (2003). A combined FT-IR microscopy and principal component analysis on softwood cell walls. *Carbohydrate Polymers, 52*(4), 449-453.

Hoshino, A., Costa-Silva, B., Shen, T.-L., Rodrigues, G., Hashimoto, A., Mark, M. T., . . . Ceder, S. (2015). Tumour exosome integrins determine organotropic metastasis. *Nature, 527*(7578), 329.

Hu, M., Wang, J., Zhao, H., Dong, S., & Cai, J. (2009). Nanostructure and nanomechanics analysis of lymphocyte using AFM: from resting, activated to apoptosis. *Journal of biomechanics, 42*(10), 1513-1519.

Huang, Z., McWilliams, A., Lui, H., McLean, D. I., Lam, S., & Zeng, H. (2003). Near-infrared Raman spectroscopy for optical diagnosis of lung cancer. *International journal of cancer, 107*(6), 1047-1052.

Izquierdo-Useros, N., Naranjo-Gómez, M., Archer, J., Hatch, S. C., Erkizia, I., Blanco, J., . . . Fernández-Figueras, M. T. (2009). Capture and transfer of HIV-1 particles by mature dendritic cells converges with the exosome-dissemination pathway. *Blood, 113*(12), 2732-2741.

Jamieson, L. E., Greaves, J., McLellan, J. A., Munro, K. R., Tomkinson, N. C., Chamberlain, L. H., . . . Graham, D. (2018). Tracking intracellular uptake and localisation of alkyne tagged fatty acids using Raman spectroscopy. *Spectrochimica Acta Part A: Molecular and Biomolecular Spectroscopy*.

Janmey, P. A., & McCulloch, C. A. (2007). Cell mechanics: integrating cell responses to mechanical stimuli. *Annu. Rev. Biomed. Eng., 9*, 1-34.

Jarvis, M., Briggs, S., & Knox, J. (2003). Intercellular adhesion and cell separation in plants. *Plant, Cell & Environment, 26*(7), 977-989.

Kacurakova, M., Capek, P., Sasinkova, V., Wellner, N., & Ebringerova, A. (2000). FT-IR study of plant cell wall model compounds: pectic polysaccharides and hemicelluloses. *Carbohydrate Polymers, 43*(2), 195-203.

Kačuráková, M., & Wilson, R. (2001). Developments in mid-infrared FT-IR spectroscopy of selected carbohydrates. *Carbohydrate Polymers, 44*(4), 291-303.

Kim, D., Lee, K., & Park, K. Y. (2016). Upgrading the characteristics of biochar from cellulose, lignin, and xylan for solid biofuel production from biomass by hydrothermal carbonization. *Journal of Industrial and Engineering Chemistry, 42*, 95-100.

Kong, W., Zhu, Y., Liang, Y., Zhang, J., Smith, F., & Yang, M. (2007). Uptake of oxytetracycline and its phytotoxicity to alfalfa (Medicago sativa L.). *Environmental Pollution, 147*(1), 187-193.

Koyner, J. L., Vaidya, V. S., Bennett, M. R., Ma, Q., Worcester, E. M., Akhter, S. A., . . . Devarajan, P. (2010). Urinary biomarkers in the clinical prognosis and early detection of acute kidney injury. *Clinical Journal of the American Society of Nephrology*, CJN. 00740110.

Krafft, C., Neudert, L., Simat, T., & Salzer, R. (2005). Near infrared Raman spectra of human brain lipids. *Spectrochimica Acta Part A: Molecular and Biomolecular Spectroscopy, 61*(7), 1529-1535.

Kristiansen, G., Yu, Y., Schlüns, K., Sers, C., Dietel, M., & Petersen, I. (2003). Expression of the cell adhesion molecule CD146/MCAM in non-small cell lung cancer. *Analytical cellular pathology, 25*(2), 77-81.

Kumar, K., Gupta, S., Baidoo, S., Chander, Y., & Rosen, C. (2005). Antibiotic uptake by plants from soil fertilized with animal manure. *Journal of environmental quality, 34*(6), 2082-2085.

Labat-Moleur, F., Steffan, A.-M., Brisson, C., Perron, H., Feugeas, O., Furstenberger, P., . . . Behr, J. (1996). An electron microscopy study into the mechanism of gene transfer with lipopolyamines. *Gene therapy, 3*(11), 1010-1017.

Larsen, K. L., & Barsberg, S. (2010). Theoretical and Raman spectroscopic studies of phenolic lignin model monomers. *The Journal of Physical Chemistry B, 114*(23), 8009-8021.

Lasch, P., Haensch, W., Naumann, D., & Diem, M. (2004). Imaging of colorectal adenocarcinoma using FT-IR microspectroscopy and cluster analysis. *Biochimica et Biophysica Acta (BBA)-Molecular Basis of Disease, 1688*(2), 176-186.

Laulagnier, K., Motta, C., Hamdi, S., Roy, S., Fauvelle, F., Pageaux, J.-F., . . . Bonnerot, C. (2004). Mast cell-and dendritic cell-derived exosomes display a specific lipid composition and an unusual membrane organization. *Biochemical Journal, 380*(Pt 1), 161.

Lee, G. Y., & Lim, C. T. (2007). Biomechanics approaches to studying human diseases. *Trends in biotechnology, 25*(3), 111-118.

Li, Q., Lee, G., Ong, C., & Lim, C. (2008). AFM indentation study of breast cancer cells. *Biochemical and biophysical research communications, 374*(4), 609-613.

Li, X., Yang, T., Lib, S., & Yu, T. (2011). *Surface-enhanced Raman spectroscopy differences of saliva between lung cancer patients and normal people.* Paper presented at the European Conference on Biomedical Optics.

Lin, J., Xu, H., Wu, Y., Tang, M., McEwen, G. D., Liu, P., . . . Zhou, A. (2013). Investigation of free fatty acid associated recombinant membrane receptor protein expression in HEK293 cells using Raman spectroscopy, calcium imaging, and atomic force microscopy. *Analytical chemistry, 85*(3), 1374-1381.

Maquelin, K., Kirschner, C., Choo-Smith, L.-P., van den Braak, N., Endtz, H. P., Naumann, D., & Puppels, G. (2002). Identification of medically relevant microorganisms by vibrational spectroscopy. *Journal of microbiological methods, 51*(3), 255-271.

Mathivanan, S., & Simpson, R. J. (2009). ExoCarta: a compendium of exosomal proteins and RNA. *Proteomics, 9*(21), 4997-5000.

Mathur, A. B., Collinsworth, A. M., Reichert, W. M., Kraus, W. E., & Truskey, G. A. (2001). Endothelial, cardiac muscle and skeletal muscle exhibit different viscous and elastic properties as determined by atomic force microscopy. *Journal of biomechanics, 34*(12), 1545-1553.

Matthäus, C., Bird, B., Miljković, M., Chernenko, T., Romeo, M., & Diem, M. (2008). Infrared and Raman microscopy in cell biology. *Methods in cell biology, 89*, 275-308.

McManus, P. S., Stockwell, V. O., Sundin, G. W., & Jones, A. L. (2002). Antibiotic use in plant agriculture. *Annual review of phytopathology, 40*(1), 443-465.

Medintz, I. L., Uyeda, H. T., Goldman, E. R., & Mattoussi, H. (2005). Quantum dot bioconjugates for imaging, labelling and sensing. *Nature materials, 4*(6), 435.

Moller, I., Marcus, S. E., Haeger, A., Verhertbruggen, Y., Verhoef, R., Schols, H., . . . Willats, W. (2008). High-throughput screening of monoclonal antibodies against plant cell wall glycans by hierarchical clustering of their carbohydrate microarray binding profiles. *Glycoconjugate journal, 25*(1), 37-48.

Monlau, F., Barakat, A., Trably, E., Dumas, C., Steyer, J.-P., & Carrère, H. (2013). Lignocellulosic materials into biohydrogen and biomethane: impact of structural features and pretreatment. *Critical reviews in environmental science and technology, 43*(3), 260-322.

Morelli, A. E., Larregina, A. T., Shufesky, W. J., Sullivan, M. L., Stolz, D. B., Papworth, G. D., . . . Watkins, S. C. (2004). Endocytosis, intracellular sorting, and processing of exosomes by dendritic cells. *Blood, 104*(10), 3257-3266.

Morse, M. A., Garst, J., Osada, T., Khan, S., Hobeika, A., Clay, T. M., . . . Delcayre, A. (2005). A phase I study of dexosome immunotherapy in patients with advanced non-small cell lung cancer. *Journal of translational medicine, 3*(1), 9.

Movasaghi, Z., Rehman, S., & ur Rehman, D. I. (2008). Fourier transform infrared (FTIR) spectroscopy of biological tissues. *Applied Spectroscopy Reviews, 43*(2), 134-179.

Nawaz, H., Bonnier, F., Meade, A. D., Lyng, F. M., & Byrne, H. J. (2011). Comparison of subcellular responses for the evaluation and prediction of the chemotherapeutic response to cisplatin in lung adenocarcinoma using Raman spectroscopy. *Analyst, 136*(12), 2450-2463.

Palmer, R. M., Ashton, D., & Moncada, S. (1988). Vascular endothelial cells synthesize nitric oxide from L-arginine. *Nature, 333*(6174), 664.

Paluszkiewicz, C., & Kwiatek, W. M. (2001). Analysis of human cancer prostate tissues using FTIR microspectroscopy and SRIXE techniques. *Journal of Molecular Structure, 565*, 329-334.

Pan, B.-T., Teng, K., Wu, C., Adam, M., & Johnstone, R. M. (1985). Electron microscopic evidence for externalization of the transferrin receptor in vesicular form in sheep reticulocytes. *The Journal of cell biology, 101*(3), 942-948.

Parolini, I., Federici, C., Raggi, C., Lugini, L., Palleschi, S., De Milito, A., . . . Molinari, A. (2009). Microenvironmental pH is a key factor for exosome traffic in tumor cells. *Journal of Biological Chemistry, 284*(49), 34211-34222.

Paula, B. M. D., Raithore, S., Manthey, J. A., Baldwin, E. A., Bai, J., Zhao, W., . . . Plotto, A. (2018). Active taste compounds in juice from oranges symptomatic for Huanglongbing (HLB) citrus greening disease. *LWT, 91*, 518-525.

Pegtel, D. M., Cosmopoulos, K., Thorley-Lawson, D. A., van Eijndhoven, M. A., Hopmans, E. S., Lindenberg, J. L., . . . Middeldorp, J. M. (2010). Functional delivery of viral miRNAs via exosomes. *Proceedings of the National Academy of Sciences, 107*(14), 6328-6333.

Pérez, M. R. V., Mendoza, M. G. G., Elías, M. G. R., González, F. J., Contreras, H. R. N., & Servín, C. C. (2016). Raman spectroscopy an option for the early detection of citrus Huanglongbing. *Applied spectroscopy, 70*(5), 829-839.

Piper, R. C., & Katzmann, D. J. (2007). Biogenesis and function of multivesicular bodies. *Annu. Rev. Cell Dev. Biol., 23*, 519-547.

Putnman, A. H. (2016). *Crisis Declaration*. Tallahasee, Florida: Florida Office of the Commisioner.

Quintás, G., Garrigues, S., Pastor, A. n., & de la Guardia, M. (2004). FT-Raman determination of Mepiquat chloride in agrochemical products. *Vibrational Spectroscopy, 36*(1), 41-46.

Rabinowits, G., Gerçel-Taylor, C., Day, J. M., Taylor, D. D., & Kloecker, G. H. (2009). Exosomal microRNA: a diagnostic marker for lung cancer. *Clinical lung cancer*, *10*(1), 42-46.

Ralph, S. A., Ralph, J., Landucci, L., & Landucci, L. (2004). NMR database of lignin and cell wall model compounds. *US Forest Prod. Lab., Madison, WI (http://ars. usda. gov/Services/docs. htm*.

Raman, C. V., & Krishnan, K. S. (1928). A new type of secondary radiation. *Nature*, *121*(3048), 501.

Raposo, G., Nijman, H. W., Stoorvogel, W., Liejendekker, R., Harding, C. V., Melief, C. J., & Geuze, H. J. (1996). B lymphocytes secrete antigen-presenting vesicles. *Journal of Experimental Medicine*, *183*(3), 1161-1172.

Rouse, B., Irey, M., Gast, T., Boyd, M., & Willis, T. (2012). *Fruit production in a southwest Florida citrus grove using the Boyd nutrient/SAR foliar spray.* Paper presented at the Proceedings of the Florida State Horticultural Society.

Ruiz-Dueñas, F. J., & Martínez, Á. T. (2009). Microbial degradation of lignin: how a bulky recalcitrant polymer is efficiently recycled in nature and how we can take advantage of this. *Microbial biotechnology*, *2*(2), 164-177.

Runge, J., Reichert, T., Fritsch, A., Käs, J., Bertolini, J., & Remmerbach, T. (2014). Evaluation of single-cell biomechanics as potential marker for oral squamous cell carcinomas: a pilot study. *Oral diseases*, *20*(3).

Saman, S., Kim, W., Raya, M., Visnick, Y., Miro, S., Saman, S., . . . Lee, N. C. (2012). Exosome-associated tau is secreted in tauopathy models and is selectively phosphorylated in cerebrospinal fluid in early Alzheimer disease. *Journal of Biological Chemistry*, *287*(6), 3842-3849.

Schulz, H., & Baranska, M. (2007). Identification and quantification of valuable plant substances by IR and Raman spectroscopy. *Vibrational Spectroscopy*, *43*(1), 13-25.

Segura, E., Guérin, C., Hogg, N., Amigorena, S., & Théry, C. (2007). CD8+ dendritic cells use LFA-1 to capture MHC-peptide complexes from exosomes in vivo. *The Journal of Immunology*, *179*(3), 1489-1496.

Sene, C. F., McCann, M. C., Wilson, R. H., & Grinter, R. (1994). Fourier-transform Raman and Fourier-transform infrared spectroscopy (an investigation of five higher plant cell walls and their components). *Plant Physiology*, *106*(4), 1623-1631.

Sharma, R. K., Wooten, J. B., Baliga, V. L., Lin, X., Chan, W. G., & Hajaligol, M. R. (2004). Characterization of chars from pyrolysis of lignin. *Fuel*, *83*(11-12), 1469-1482.

Shetty, G., Kendall, C., Shepherd, N., Stone, N., & Barr, H. (2006). Raman spectroscopy: elucidation of biochemical changes in carcinogenesis of oesophagus. *British journal of cancer, 94*(10), 1460.

Shimomura, O., Johnson, F. H., & Saiga, Y. (1962). Extraction, purification and properties of aequorin, a bioluminescent protein from the luminous hydromedusan, Aequorea. *Journal of Cellular Physiology, 59*(3), 223-239.

Sijtsema, N. M., Wouters, S. D., De Grauw, C. J., Otto, C., & Greve, J. (1998). Confocal direct imaging Raman microscope: design and applications in biology. *Applied spectroscopy, 52*(3), 348-355.

Singh, R. P., & Ramarao, P. (2012). Cellular uptake, intracellular trafficking and cytotoxicity of silver nanoparticles. *Toxicology letters, 213*(2), 249-259.

Skog, J., Würdinger, T., Van Rijn, S., Meijer, D. H., Gainche, L., Curry Jr, W. T., . . . Breakefield, X. O. (2008). Glioblastoma microvesicles transport RNA and proteins that promote tumour growth and provide diagnostic biomarkers. *Nature cell biology, 10*(12), 1470.

Smith, V. L., Cheng, Y., Bryant, B. R., & Schorey, J. S. (2017). Exosomes function in antigen presentation during an in vivo Mycobacterium tuberculosis infection. *Scientific reports, 7*, 43578.

Socrates, G. (2001). *Infrared and Raman characteristic group frequencies: tables and charts*: John Wiley & Sons.

Soliman, M., & Tetard, L. (2017). Probing Chemical and Physical Properties of Poplar Tension Wood Using Confocal Raman Microscopy and Pulsed Force Mode Atomic Force Microscopy. *MRS Advances, 2*(19-20), 1103-1109.

Srikun, D., Albers, A. E., Nam, C. I., Iavarone, A. T., & Chang, C. J. (2010). Organelle-targetable fluorescent probes for imaging hydrogen peroxide in living cells via SNAP-Tag protein labeling. *Journal of the American Chemical Society, 132*(12), 4455-4465.

Stehfest, K., Toepel, J., & Wilhelm, C. (2005). The application of micro-FTIR spectroscopy to analyze nutrient stress-related changes in biomass composition of phytoplankton algae. *Plant Physiology and Biochemistry, 43*(7), 717-726.

Steppe, K., Dzikiti, S., Lemeur, R., & Milford, J. R. (2006). Stomatal oscillations in orange trees under natural climatic conditions. *Annals of Botany, 97*(5), 831-835.

Stockwell, V., & Duffy, B. (2012). Use of antibiotics in plant agriculture.

Stone, N., Kendall, C., Smith, J., Crow, P., & Barr, H. (2004). Raman spectroscopy for identification of epithelial cancers. *Faraday discussions, 126*, 141-157.

Subra, C., Laulagnier, K., Perret, B., & Record, M. (2007). Exosome lipidomics unravels lipid sorting at the level of multivesicular bodies. *Biochimie, 89*(2), 205-212.

Sun, L., Simmons, B. A., & Singh, S. (2011). Understanding tissue specific compositions of bioenergy feedstocks through hyperspectral Raman imaging. *Biotechnology and bioengineering, 108*(2), 286-295.

Suresh, S., Spatz, J., Mills, J., Micoulet, A., Dao, M., Lim, C., . . . Seufferlein, T. (2005). Connections between single-cell biomechanics and human disease states: gastrointestinal cancer and malaria. *Acta biomaterialia, 1*(1), 15-30.

Tamm, L. K., & Tatulian, S. A. (1997). Infrared spectroscopy of proteins and peptides in lipid bilayers. *Quarterly reviews of biophysics, 30*(4), 365-429.

Taylor, D. D., & Gercel-Taylor, C. (2008). MicroRNA signatures of tumor-derived exosomes as diagnostic biomarkers of ovarian cancer. *Gynecologic oncology, 110*(1), 13-21.

Tetard, L., Passian, A., Farahi, R., Davison, B. H., Jung, S., Ragauskas, A., . . . Thundat, T. (2011). Nanometrology of delignified Populus using mode synthesizing atomic force microscopy. *Nanotechnology, 22*(46), 465702.

Tetard, L., Passian, A., Farahi, R., Kalluri, U., Davison, B., & Thundat, T. (2010). Spectroscopy and atomic force microscopy of biomass. *Ultramicroscopy, 110*(6), 701-707.

Tetard, L., Passian, A., Farahi, R., Thundat, T., & Davison, B. H. (2015). Opto-nanomechanical spectroscopic material characterization. *Nature nanotechnology, 10*(10), 870.

Théry, C., Boussac, M., Véron, P., Ricciardi-Castagnoli, P., Raposo, G., Garin, J., & Amigorena, S. (2001). Proteomic analysis of dendritic cell-derived exosomes: a secreted subcellular compartment distinct from apoptotic vesicles. *The Journal of Immunology, 166*(12), 7309-7318.

Théry, C., Zitvogel, L., & Amigorena, S. (2002). Exosomes: composition, biogenesis and function. *Nature Reviews Immunology, 2*(8), 569.

Touhami, A., Nysten, B., & Dufrêne, Y. F. (2003). Nanoscale mapping of the elasticity of microbial cells by atomic force microscopy. *Langmuir, 19*(11), 4539-4543.

Tuma, R. (2005). Raman spectroscopy of proteins: from peptides to large assemblies. *Journal of Raman Spectroscopy, 36*(4), 307-319.

Vaher, M., & Koel, M. (2003). Separation of polyphenolic compounds extracted from plant matrices using capillary electrophoresis. *Journal of chromatography A, 990*(1-2), 225-230.

Valadi, H., Ekström, K., Bossios, A., Sjöstrand, M., Lee, J. J., & Lötvall, J. O. (2007). Exosome-mediated transfer of mRNAs and microRNAs is a novel mechanism of genetic exchange between cells. *Nature cell biology, 9*(6), 654.

Venkatachalam, P., Priyanka, N., Manikandan, K., Ganeshbabu, I., Indiraarulselvi, P., Geetha, N., . . . Sharma, N. (2017). Enhanced plant growth promoting role of phycomolecules coated zinc oxide nanoparticles with P supplementation in cotton (Gossypium hirsutum L.). *Plant Physiology and Biochemistry, 110*, 118-127.

Verhoeckx, K., Bijlsma, S., de Groene, E. M., Witkamp, R. F., van der Greef, J., & Rodenburg, R. J. (2004). A combination of proteomics, principal component analysis and transcriptomics is a powerful tool for the identification of biomarkers for macrophage maturation in the U937 cell line. *Proteomics, 4*(4), 1014-1028.

Vidaver, A. K. (2002). Uses of antimicrobials in plant agriculture. *Clinical infectious diseases, 34*(Supplement_3), S107-S110.

Wagner, M., & Mueller, T. (2016). High-Resolution Nanochemical Mapping of Soft Materials. *Microscopy Today, 24*(3), 44-51.

Wang, D., Liu, S., Trummer, B. J., Deng, C., & Wang, A. (2002). Carbohydrate microarrays for the recognition of cross-reactive molecular markers of microbes and host cells. *Nature biotechnology, 20*(3), 275.

Wang, H., Wang, H.-C., & Huang, Y.-J. (1997). Microscopic FTIR studies of lung cancer cells in pleural fluid. *Science of the Total Environment, 204*(3), 283-287.

Wang, J., Boy, R., Nguyen, N. A., Keum, J. K., Cullen, D. A., Chen, J., . . . Tetard, L. (2017). Controlled Assembly of Lignocellulosic Biomass Components and Properties of Reformed Materials. *ACS Sustainable Chemistry & Engineering, 5*(9), 8044-8052.

Whelan, D. R., Bambery, K. R., Heraud, P., Tobin, M. J., Diem, M., McNaughton, D., & Wood, B. R. (2011). Monitoring the reversible B to A-like transition of DNA in eukaryotic cells using Fourier transform infrared spectroscopy. *Nucleic acids research, 39*(13), 5439-5448.

Wolfers, J., Lozier, A., Raposo, G., Regnault, A., Théry, C., Masurier, C., . . . Tursz, T. (2001). Tumor-derived exosomes are a source of shared tumor rejection antigens for CTL cross-priming. *Nature medicine, 7*(3), 297.

Wood, B. R., Quinn, M. A., Tait, B., Ashdown, M., Hislop, T., Romeo, M., & McNaughton, D. (1998). FTIR microspectroscopic study of cell types and potential confounding variables in screening for cervical malignancies. *Biospectroscopy, 4*(2), 75-91.

Wubbolts, R., Leckie, R. S., Veenhuizen, P. T., Schwarzmann, G., Möbius, W., Hoernschemeyer, J., . . . Stoorvogel, W. (2003). Proteomic and biochemical analyses of human B cell-derived exosomes Potential implications for their function and multivesicular body formation. *Journal of Biological Chemistry, 278*(13), 10963-10972.

Xu, F., Yu, J., Tesso, T., Dowell, F., & Wang, D. (2013). Qualitative and quantitative analysis of lignocellulosic biomass using infrared techniques: a mini-review. *Applied Energy, 104*, 801-809.

Xu, L., Yan, W., Ma, W., Kuang, H., Wu, X., Liu, L., . . . Xu, C. (2015). SERS encoded silver pyramids for attomolar detection of multiplexed disease biomarkers. *Advanced Materials, 27*(10), 1706-1711.

Yang, D., Castro, D. J., El-Sayed, I. H., El-Sayed, M. A., Saxton, R. E., & Zhang, N. Y. (1995). *Fourier-transform infrared spectroscopic comparison of cultured human fibroblast and fibrosarcoma cells.* Paper presented at the Optical Tomography, Photon Migration, and Spectroscopy of Tissue and Model Media: Theory, Human Studies, and Instrumentation.

Yang, T., Martin, P., Fogarty, B., Brown, A., Schurman, K., Phipps, R., . . . Bai, S. (2015). Exosome delivered anticancer drugs across the blood-brain barrier for brain cancer therapy in Danio rerio. *Pharmaceutical research, 32*(6), 2003-2014.

Yang, T., Zhang, Z., Zhao, B., Hou, R., Kinchla, A., Clark, J. M., & He, L. (2016). Real-time and in situ monitoring of pesticide penetration in edible leaves by surface-enhanced Raman scattering mapping. *Analytical chemistry, 88*(10), 5243-5250.

Yeung, K. Y., & Ruzzo, W. L. (2001). Principal component analysis for clustering gene expression data. *Bioinformatics, 17*(9), 763-774.

Zhang, X., Roeffaers, M. B., Basu, S., Daniele, J. R., Fu, D., Freudiger, C. W., . . . Xie, X. S. (2012). Label-Free Live-Cell Imaging of Nucleic Acids Using Stimulated Raman Scattering Microscopy. *ChemPhysChem, 13*(4), 1054-1059.

Zheng, J., Hernandez, J. M., Doussot, A., Bojmar, L., Zambirinis, C. P., Costa-Silva, B., . . . Askan, G. (2018). Extracellular matrix proteins and carcinoembryonic antigen-related cell adhesion molecules characterize pancreatic duct fluid exosomes in patients with pancreatic cancer. *HPB*.

zu Heringdorf, D. M., Lass, H., Kuchar, I., Lipinski, M., Alemany, R., Rümenapp, U., & Jakobs, K. H. (2001). Stimulation of intracellular sphingosine-1-phosphate production by G-protein-coupled sphingosine-1-phosphate receptors. *European journal of pharmacology, 414*(2-3), 145-154.